# DEVELOPMENT AND CHARACTERIZATION OF (CARBONATED) HYDROXYAPATITE, AKERMANITE INVOLVING POLYCAPROLACTONE SCAFFOLDS

A THESIS SUBMITTED TO
THE GRADUATE SCHOOL OF NATURAL AND APPLIED SCIENCES
OF
MIDDLE EAST TECHNICAL UNIVERSITY

BY

GERÇEM ALTUNORDU

IN PARTIAL FULFILLMENT OF THE REQUIREMENTS
FOR
THE DEGREE OF MASTER OF SCIENCE
IN
BIOMEDICAL ENGINEERING

SEPTEMBER 2019

Approval of the thesis:

**DEVELOPMENT AND CHARACTERIZATION OF (CARBONATED) HYDROXYAPATITE, AKERMANITE INVOLVING POLYCAPROLACTONE SCAFFOLDS**

submitted by **GERÇEM ALTUNORDU** in partial fulfillment of the requirements for the degree of **Master of Science in Biomedical Engineering Department, Middle East Technical University** by,

Prof. Dr. Halil Kalıpçılar
Dean, Graduate School of **Natural and Applied Sciences** _____

Assoc. Prof. Dr. Ergin Tönük
Head of Department, **Biomedical Engineering** _____

Prof. Dr. Dilek Keskin
Supervisor, **Engineering Sciences Dept., METU** _____

Prof. Dr. Zafer Evis
Co-Supervisor, **Engineering Sciences Dept., METU** _____

**Examining Committee Members:**

Prof. Dr. Ayşen Tezcaner
Engineering Sciences Dept., METU _____

Prof. Dr. Dilek Keskin
Engineering Sciences Dept., METU _____

Prof. Dr. Zafer Evis
Engineering Sciences Dept., METU _____

Prof. Dr. Sreeparna Banerjee
Biological Sciences Dept., METU _____

Assist. Prof. Dr. Bengi Yılmaz
Biomaterials Dept., University of Health Sciences _____

Date: 09.09.2019

**I hereby declare that all information in this document has been obtained and presented in accordance with academic rules and ethical conduct. I also declare that, as required by these rules and conduct, I have fully cited and referenced all material and results that are not original to this work.**

Name, Surname: Gerçem Altunordu

Signature:

# ABSTRACT

## DEVELOPMENT AND CHARACTERIZATION OF (CARBONATED) HYDROXYAPATITE, AKERMANITE INVOLVING POLYCAPROLACTONE SCAFFOLDS

Altunordu, Gerçem
Master of Science, Biomedical Engineering
Supervisor: Prof. Dr. Dilek Keskin
Co-Supervisor: Prof. Dr. Zafer Evis

September 2019, 95 pages

Bone tissue loss or damage can occur due to accidents, injuries and diseases (osteomyelitis, osteosarcaoma, osteoporosis, etc.). Bone tissue engineering (BTE) aims to develop biomaterials that enhance the regeneration of bone tissue. Therefore, scaffolds for BTE should be biocompatible and bioactive; enabling strong communication with bone tissue. Bioceramics are a group of biomaterials that resemble to native bone mineral and improve bioactivity of BTE scaffolds. Considering these hydroxyapatite (HA), carbonated hydroxyapatite (CHA) and akermanite (AKR) bioceramics were synthesized and their optimum combination was determined to be used as BTE scaffolds. Bioactivities of all bioceramics were good. However, it was seen that AKR makes the ambient pH of the incubation medium basic. Therefore, 90% HA-10% AKR and 90% CHA-10% AKR bioceramic groups were prepared and compared with only HA or CHA containing groups. Bioceramic-polymer composite scaffolds were prepared by wet electrospinning of poly ε-caprolactone (PCL) solution loaded with these bioceramics (10% w/w) and then characterized for degradation, swelling and microstructural properties. Scaffolds containing CHA and AKR were shown to highly support apatite formation. Additionaly, cell proliferation and osteogenic activity were studied with bone cells

(Saos-2). Among all, PCL scaffolds containing 90%HA-10%AKR and 90%CHA-10%AKR minerals supported better cell proliferation. It was observed that all groups induced cell differentiation with apatite layer formation. Therefore, all scaffolds groups are considered to be promising for use in bone tissue engineering applications.

Keywords: Hydroxyapatite, Akermanite, Bone Tissue Engineering, Electrospinning, PCL

# ÖZ

## POLİKAPROLAKTON İSKELELERİ İÇEREN (KARBONATLI) HİDROKSİAPATİTİN, AKERMANİTİN GELİŞTİRİLMESİ VE KARAKTERİZASYONU

Altunordu, Gerçem
Yüksek Lisans, Biyomedikal Mühendisliği
Tez Danışmanı: Prof. Dr. Dilek Keskin
Ortak Tez Danışmanı: Prof. Dr. Zafer Evis

Eylül 2019, 95 sayfa

Kemik doku kaybı veya hasarı kazalardan, yaralanmalardan ve hastalıklardan (osteomiyelit, osteosarkom, osteoporoz vd.) dolayı olabilir. Kemik doku mühendisliği (BTE), kemik doku yenilenmesini geliştiren biyomalzemeler geliştirmeyi amaçlamaktadır. Dolayısıyla, BTE için olan iskeleler, biyouyumlu ve biyoaktif olmalıdırlar; kemik dokusu ile güçlü iletişimi sağlar. Biyoseramikler doğal kemik mineraline benzeyen ve BTE iskelelerinin biyoaktivitesini artıran bir grup biyomateryallerdir. Bunlar göz önünde bulundurularak, hidroksiapatit (HA), karbonatlı hidroksiapatit (CHA) ve akermanit (AKR) biyoseramikleri sentezlendi ve BTE iskelelerinde kullanılmak üzere optimum kombinasyonları belirlendi. Tüm biyoseramiklerin biyoaktiviteleri iyiydi. Ancak, AKR'nin inkübasyon ortamının pH'sini bazik yaptığı görülmüştür. Bu nedenle, %90HA-%10AKR ve %90CHA-%10AKR biyoseramik grupları hazırlanmış ve sadece HA ve CHA içeren gruplarla karşılaştırılmıştır. Biyoseramik-polimer kompozit iskeleleri bu biyoseramiklerle yüklenen (ağırlıkça %10) poli ε-kaprolakton (PCL) çözeltinin ıslak elektroeğirmesiyle hazırlanmış ve degredasyon, şişme ve mikroyüzeysel özellikler bakımından karakterize edilmişlerdir. CHA ve AKR içeren iskelelerin yüksek oranda apatit oluşumunu destekledikleri görülmüştür. İlave olarak, hücre çoğalması ve osteojenik

aktivite kemik hücreleriyle (Saos-2) çalışılmıştır. Tüm iskelelerin arasında, %90HA-%10AKR ve %90CHA-%10AKR minerallerini içeren PCL iskelelerinin hücre çoğalması daha iyiydi. Bütün grupların apatit katman oluşturarak osteojenik aktivite sağladıkları incelenmiştir. Sonuç olarak, tüm iskele gruplarının kemik dokusu mühendisliği uygulamalarında kullanım için umut verici olduğu düşünülmektedir.

Anahtar Kelimeler: Hidroksiapatit, Akermanit, Kemik Doku Mühendisliği, Electrospin, PCL

To my dear mother Berrin Altunordu for contribution to whole my education and unconditional love…

## ACKNOWLEDGEMENTS

I would like to express my sincere gratitude to my supervisor Prof. Dr. Dilek Keskin and cosupervisor Prof. Dr. Zafer Evis for their guidance, advice, criticism, encouragement and insight throughout the research.

Similar profound gratitude goes to Prof. Dr. Ayşen Tezcaner for her valuable suggestions, comments and sound advice.

Many friends have helped me stay sane through the difficult times. I greatly valuable their friendship, emotional supports and for all the fun we have had during all these years. I would like to thank Gülçin Çiçek and Deniz Atila for deepest and unconditional friendships and valuable guidance in all the time of writing this thesis.

I would like to thank my lab friend Ali Moutameni for help me in mechanical tests and sharing knowledge to me.

I would like to thank my other lab mates for their helps.

I would like to thank my dear first dormitory friend Damla Özgün for her sincere friendship, encouragement and valuable thoughts.

Similar thanks go to my sweet friends Öznur İlgen, Ayfer Acar, Duygu Çelik, Şeyma Fetvacı and Seden Ayvalı for their love and faith to me. Thank you for all the laughter moments my dear friends.

I would like to thank my dear and sweet colleague friend Ebru Aygül for her helps, encouragements and intimate friendship especially in the last three months.

Finally, I would like to thank to my family for their love, faith and encouragement.

## TABLE OF CONTENTS

## LIST OF TABLES

TABLES

## LIST OF FIGURES

FIGURES

## LIST OF ABBREVIATIONS

ABBREVIATIONS

| | |
|---|---|
| AKR | Akermanite |
| ALP | Alkaline Phosphatase |
| BTE | Bone Tissue Engineering |
| CHA | Carbonated Hydroxyapatite |
| EDX | Energy Dispersive X-Ray Spectroscopy |
| FTIR | Fourier Transform Infrared |
| HA | Hydroxyapatite |
| HAECs | Human Aortic Endothelial Cells |
| hBMSCs | Human Bone Marrow Stromal Osteoprogenitor Cells |
| ICDD | International Center for Diffraction Data |
| JCPDS | Joint Committee on Powder Diffraction |
| MSCs | Mesenchymal Stem Cells |
| n | Number of samples/measurements |
| OC | Osteocalcin |
| ON | Osteonectin |
| OP | Osteopontin |
| PBS | Phosphatase Buffered Solution |
| PCL | Poly ε-caprolactone |
| PGA | Polyglycolic Acid |

| | |
|---|---|
| PLGA | Poly-DL-Lactic-co-Glycolic Acid |
| PLLA | Poly-L-Lactic acid |
| pNPP | P-Nitrophenol |
| PS | Polystyrene |
| PVP | Polyvinylpyrolidone |
| SBF | Simulated Body Fluid |
| SEM | Scanning Electron Microscope |
| SR | Swelling Ratio |
| VEGF | Vascular Endothelial Growth Factor |
| XRD | X-Ray Diffraction |

# CHAPTER 1

# INTRODUCTION

## 1.1. Bone

Bone, a highly vascularized connective tissue, supports and protects various internal organs (Soundarya et al., 2018a). Bone tissue also has a hierarchical structure in its anatomy as shown in Figure 1.1.

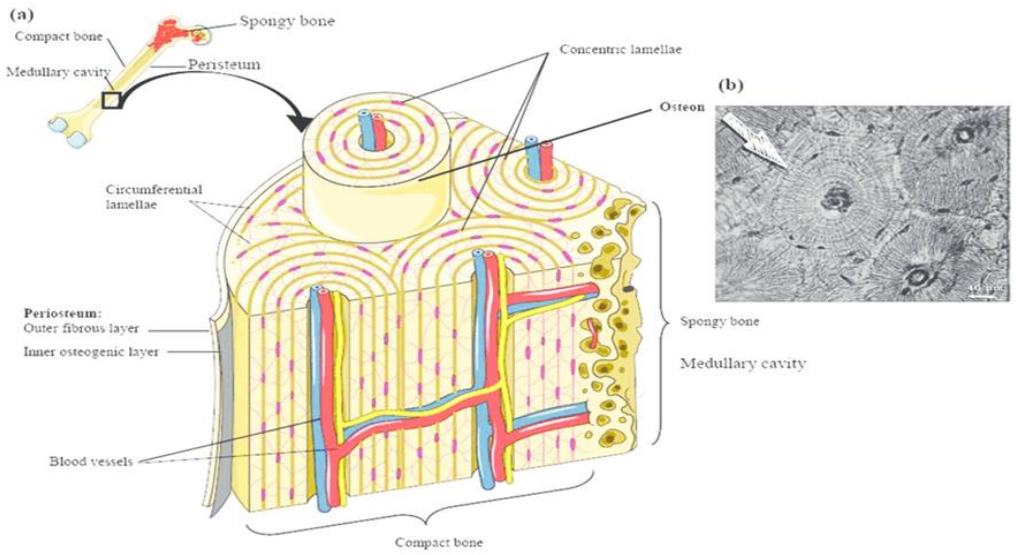


*Figure 1.1.* Schematic representation of compact bone anatomy. (a) Cross-sectional illustration of compact bone with basic structural units. (b) Micrograph of the osteon with concentric lamellae and central canals (Osta, 2014).

There are mainly five different types of bones in human body in terms of their shapes: Long, short, flat, sesamoid and irregular bones. Although their functionalities are different, cortical and trabecular bones are two main forms of them (Wang et al., 2009)

(Figure 1.2). Whereas the cortical bone induces mechanical integrity and protection, trabecular bone exerts movements of joints and limbs (Soundarya et al., 2018a).

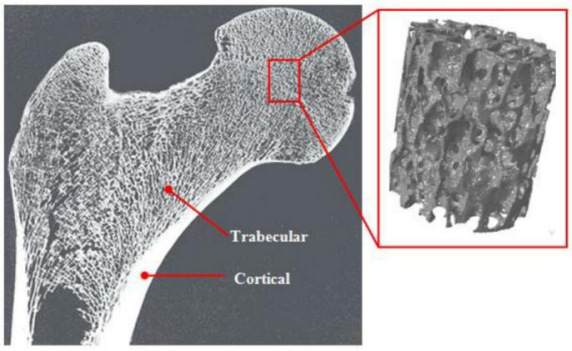


*Figure 1.2.* Cross-section of human femur showing trabecular and cortical bone (Hambli & Hattab, 2013).

Formation of stem cells by "bone marrow" provides an extra property to the bone tissue (Sethu et al., 2017). Bone marrow that is present in the spongy phase has an important responsibility: Accommodation and maintenance of hematopoietic and mesenchymal stem cell niche and osteoprogenitor cells (Shanmugam & Roman, 2008) (Figure 1.3). Osteoprogenitor cells play an important role in bone resorption and formation.

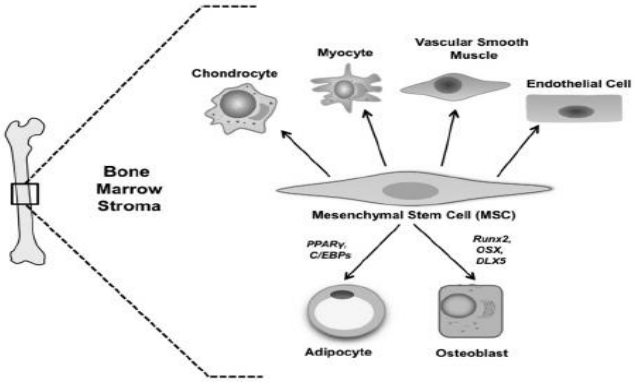


*Figure 1.3.* Differentiation of the bone marrow mesenchymal stem cells into multiple cell types such as chondrocyte and myocyte. Differentiation from MSCs needs activation of several transcription factors such as Runx2, OSX and DLXS (Shanmugam & Roman, 2008).

### 1.1.1. Bone Matrix

Bone matrix contains predominantly osteoid and porous collagen. Calcium and phosphate ions settle into these pores by crystallizing and form an inorganic mineral named hydroxyapatite ($Ca_5(PO_4)_3(OH)$) with minute amounts of other minerals (Soundarya et al., 2018a). Moreover, most of the organic phase is type I collagen (Bala & Seeman, 2015). Osteoprogenitor cells are responsible for secreting this and other bone proteins. Type I collagen has a cross-linked triple helix structure. Furthermore, type I collagen induces mineralization due to its nucleation property in bone tissue. At the end of this mineralization, mineralized collagen fibrils form and finally create lamellae. Thus, type I collagen can be seen as the major component for bone development. The hierarchical structure of the bone structure with mineralization of collagen fibrils can be seen in Figure 1.4.

Bone matrix has also non-collagenous proteins namely, osteocalcin (OC), osteonectin (ON), osteopontin (OP) and thrombospondin (Bala & Seeman, 2015; Soundarya et al., 2018a). They have crucial role in bone formation and crystallization. Their functions are summarized in Table 1.1.

Table 1.1. *Functions of some non-collagenous proteins in bone tissue.*

| Type of Non-collagenous Protein | Function | References |
|---|---|---|
| Osteocalcin | Regulation of bone formation<br>Binding of calcium | (Marshall et al., 2014)<br>(Hall, 2015) |
| Osteopontin | Cell attachment, calcium binding<br>Regulation of bone remodelling | (Glorieux et al., 2012) |
| Osteonectin | Modulating of cell attachment<br>Providing cell differentiation<br>Apatite and matrix protein binding | (Hochberg et al., 2015) |
| Decorin | Collagen fibrillogenesis<br>Growth factor binding | (Boskey&Robey, 2013) |
| Bone sialoprotein | Cell attachment<br>Calcium binding<br>Regulation of bone formation | (Robey, 2008) |
| Matrix-GLA-protein | Inhibition of matrix mineralization | (Atkins et al., 2011) |
| Thrombospontin | Cell attachment<br>Growth factor binding<br>Hydoxyapatite formation | (Robey, 2008) |

### 1.1.2. Ossification or Osteogenesis

Bone formation is described as ossification or osteogenesis. As mentioned before, bone tissue has hierarchical structure. Formation of this hierarchical structure is initiated with mineralization of collagen fibrils (Figure 1.4) (Liu et al., 2016). In mineralized bone matrix, there are four main types of cells: Osteoblasts, osteoclasts, osteocytes and bone lining cells. Osteoblasts produce new bone matrix in ossification process by making and releasing the proteins and other organic components of the matrix. Osteoclasts absorb and remove bone matrix by means of acids and protein

digesting enzymes they secrete. They have crucial role in regulating calcium and phosphate concentration in body fluids. Osteocytes have two main functions. Firstly, they maintain the protein and mineral content of the surrounding matrix. Secondly, they are responsible for repairing damaged bone. Bone lining cells are the source of active osteoblast cells which help proliferation and differentiation. Shortly, these four types of bone cells regulate bone formation and resorption dynamically (Stevens, 2008) (Bala & Seeman, 2015) (Liu et al., 2016).

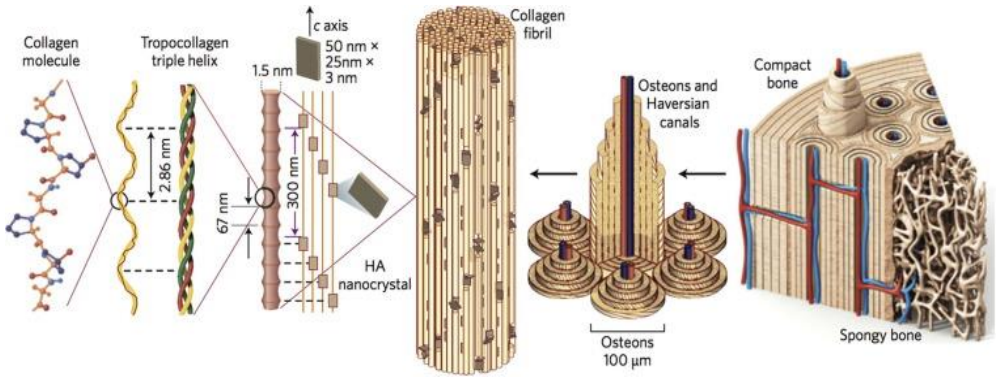


*Figure 1.4.* Schematic representation of hierarchical bone structure with mineralization of collagen fibrils (Liu et al., 2016).

### 1.1.3. Hydroxyapatite

Hydroxyapatite (HA), is the primary phase of the inorganic part of the bone with approximately 70% by weight. Due to the presence of hydroxyl groups, ($-OH^-$), it is named as HA. HA has a crystal structure with $Ca^{2+}$, $PO_4^{3-}$ and $OH^-$ ions (Figure 1.5). Ca/P molar ratio in the stoichiometric HA is 1.67 (Venkatesan et al., 2015).

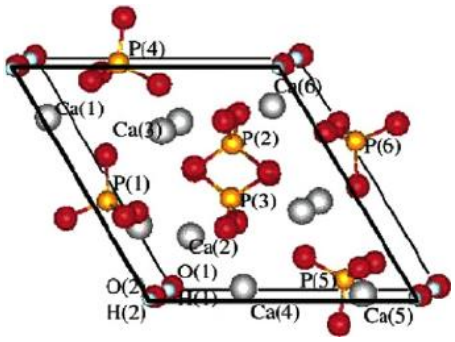


*Figure 1.5.* Hexagonal crystal structure of HA (Manafi et al., 2008).

In the structure of HA, an array of $PO_4$ tetrahedra is held together by $Ca^{2+}$ ions. $Ca^{2+}$ ions are in two different sites, the adjacent $OH^-$ ions occur in opposite directions. $Ca^{2+}$ ions have an ability of triggering the coordination between HA and collagen molecules, because the mineral and collagen matrix are hydrated by the water (9%, w/w of total bone tissue) (Dorozhkin, 2015). In bone tissue, there is an interaction between $Ca^{2+}$ and collagen molecules. As a result of this situation, while bone is growing, its mineral phase may coat the lamella. Step by step, these lamellae form the osteons and HA deposition gives compressive strength to the bone tissue.

### 1.1.4. Carbonated Hydroxyapatite

Synthetic HA is widely used in artificial bone constructs in certain cases due to its resemblance to the inorganic part of hard tissues. However, in these applications, obtained efficiency is not as successful as natural bone. Therefore, carbonated HA (CHA), is the most preferred material for hard tissues such as bone, dentine and enamel (Ezekiel et al., 2018). In native bone, there is a small amount of carbonate (content is about 2-8 wt% of total bone mass), changing with age and it may substitute the phosphate or hydroxyl groups (Okada & Matsumoto, 2015). Some studies showed that CHA has lower crystallinity than HA. This case provides improved solubility in bioactivity studies (Ezekiel et al., 2018).

### 1.1.5. Bone Defects

Unlike many other tissues in body, bones have a unique property in terms of regeneration and remodeling in response to some defects (Xing et al., 2018; Soundarya et al., 2018a). “Bone remodeling” is a specific term and it means triggering of the bone daily by the osteogenic cells. In other words, bone remodeling expresses the formation of the new bone tissue (Soundarya et al., 2018b) (Figure 1.6).

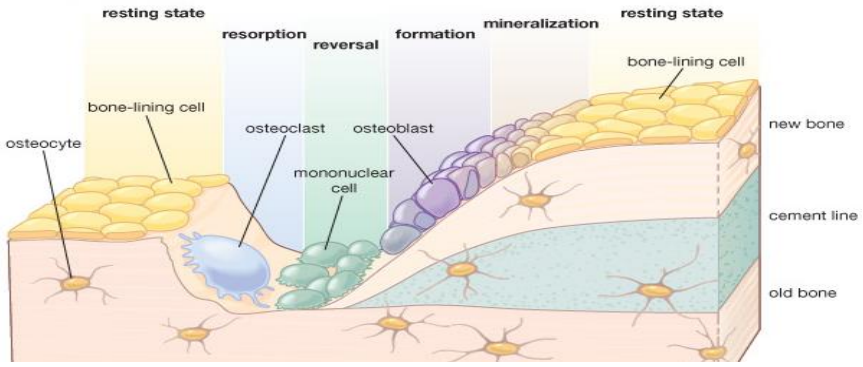


*Figure 1.6.* Representation of bone remodeling. All of the bone cells work together in this process (From Encyclopedia of Britannica, [https://www.britannica.com/science/bone-remodeling]).

In some situation such as long-bone injuries, bone tumors, bone fractures (Figure 1.7), periodontitis, osteomyelitis, heavy fractures, arthrosis and osteoporosis, the required bone regeneration and remodeling exceed the natural potential for its self-healing (Wang et al., 2009; Soundarya et al., 2018b). The mentioned bone defects lead to bone weakness and brittleness. Therefore, bone fractures become inevitable.

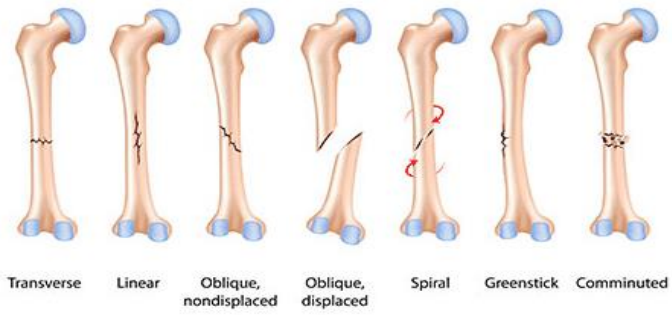


*Figure 1.7.* Types of the bone fractures (Elmagd, 2016).

A disorder of the development of bone and cartilage is called osteochondrodysplasia. There are some sources of bone defects such as genetic malformations and accidents. For instance, genetic disorders of bone contain osteogenesis imperfections that may influence specific or multiple regions of a skeleton (Soundarya et al., 2018a).

### 1.2. Bone Tissue Engineering

In recent years, bone repair and regeneration have become a serious challenge in orthopedic applications due to the increase in clinical bone defects. Some common applications such as autografts and allografts are two types of the therapy methods for bone defects (Wang et al., 2009). However, these techniques have many major negative outcomes. For example, autograft, bones obtained from another anatomical site in the same subject, provides the excellent standard for the bone repair and regeneration; however, this surgical technique have many challenges such as the possibility of donor site morbidity, limitation of donor bone supply, anatomical and structural complications (Diba et al., 2014). In addition, allograft, bones from donors, can lead to some problems such as disease transmission and immunogenic responses (Wang et al., 2009; Diba et al., 2014).

Due to these possible problems about autograft and allograft methods, most researchers have investigated use of different biomaterials. For example, metallic materials like cobalt chrome alloys, stainless steel, titanium and its alloys were used

for treatment of bone defects (Soundarya et al., 2018b). However, these materials can be immunogenic and non-bioresorbable. Therefore, many researchers have applied nanotechnology in regenerative medicine, nanofiber scaffolding, modification of nanotopography of nanoparticles and scaffolds (Sethu et al., 2017; Soundarya et al., 2018a). Hence, bone-tissue engineering has attracted attention in terms of bone repair and regeneration. In general, bone-tissue engineering scaffolds are designed to mimic the structural and biological functions of a naturally occurring extracellular matrix with respect to chemical composition and physical structure (Wang et al., 2014). One of the approaches of the bone-tissue engineering is to combine a biodegradable scaffold and living cells to grow tissue in vitro prior to implantation of the subject. To achieve successful results in bone-tissue engineering, usage of some chemicals like phytochemicals (Soundarya et al., 2018a), proteins, peptides and cells to enhance bone formation, and affect osteoblast and osteoclast differentiation are needed. They may provide bioactivity property to scaffolds.

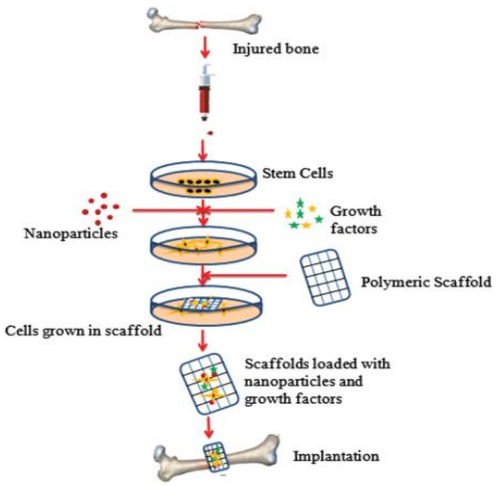


*Figure 1.8.* A scheme describing possible components and general approach for bone tissue engineering (Shukla et al., 2017).

There are three vital topics in bone-tissue engineering: Scaffolding matrix, stem cells, and growth factors or bioactive molecules such as proteins, drugs, and phytochemicals (Soundarya et al., 2018a).

In bone-tissue engineering, scaffolds should have many properties such as high porosity, a macroporous network for in vitro cell migration, adhesion, proliferation, and further tissue growth, biocompatibility and biodegradability, sufficient mechanical strength (Diba et al., 2014; Soundarya et al., 2018b). In order to use the scaffolds in bone-tissue engineering efficiently, scaffold has to possess flexibility in manufacturing to required final form, i.e. enabling fabrication in 3D-structures (Soundarya et al., 2018b). Porosity of the biomaterial manufactured into desired structures has to induce cell adhesion, cell infiltration, and growth so it can be said that there is a good interconnection among the pores. This means that the fabricated biomaterial possess attachment with bone cell. Also, another important required characteristic of the 3D-structured biomaterial is rate of degradation; they should have proportionality in the rate of formation of the new bone and the rate of the degradation. In here, there is another crucial point: the 3D-structured biomaterial's degradation byproducts must not lead to inflammation and toxicity in surrounding tissues or the whole body of the host (Niranjan et al., 2013; Motamedian et al., 2015).

### 1.2.1. Biomaterials in Bone Tissue Engineering

#### 1.2.1.1. Natural Polymers

Polymers are basically classified as natural and synthetic according to their origin (Logithkumar et al., 2016). Due to good biocompatibility and biodegradability, natural polymers are ideal materials to be used in bone-tissue engineering (Chen & Liu, 2016). Some properties of polymer based scaffolds such as porosity, charge, mechanical strength and degradation can be controlled by tuning the polymer concentrations and conditions. Collagen, hyaluronic acid, chitosan, alginate and fibroin are examples of some natural polymers used in the development of scaffolds for bone-tissue engineering. Collagen is the most abundant protein in mammals and the main

structural component of the extracellular matrix, with (Gly-X-Y)n repeating units longer than 1400 amino acid residues and with three residues per one helical turn structure (Lee et al., 2001) (Figure 1.9). The X and Y may be proline or 4 hydroxyproline. In bone-tissue engineering, to produce electrospun fibers or scaffold matrices Collagen and its derivative were obtained from various sources such as marine organisms, and ruminants (Wang et al 2014; Logithkumar et al., 2016; Soundarya et al., 2018b). Collagen was used in many bone tissue engineering studies. For example, collagen-hydroxyapatite scaffolds were produced by freeze-casting method and then viability and attachment of bone marrow stromal cells were evaluated in vitro (Villa et al., 2015). It was shown that collagen-HA scaffold supports osteogenesis robustly. In addition, whereas pure synthetic HA do not degrade after 6 years of implantation with expanded bone marrow stromal cells in humans, collagen-HA scaffolds could degrade faster than pure HA (Marcacci et al., 2007).

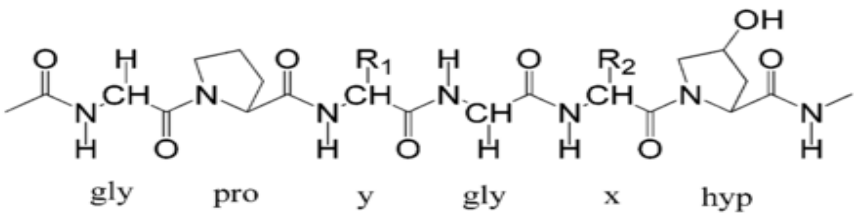


*Figure 1.9.* Chemical structure of a part of Collagen Type I showing Groups of X and Y can be proline or 4-hydroxyproline (Liao et al., 2004).

Another natural polymer highly used in bone-tissue engineering is Hyaluronic acid which is a polysaccharide mainly made up of residues of D-glucuronic acid and N-acetyl glucosamine (Liao et al., 2004) (Figure 1.10). It is mainly found in the connective tissues. Hyaluronic acid represents great properties for bone-tissue

engineering such as high viscosity, elasticity, biocompatibility, non-immunogenicity and biodegradability.

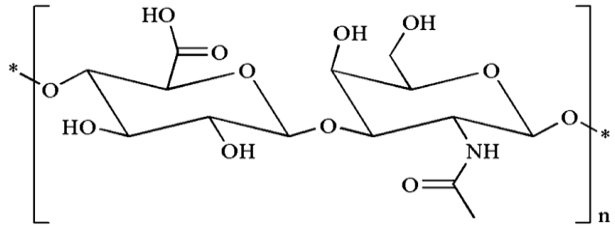


*Figure 1.10.* Chemical structure of hyaluronic acid (Wang et al., 2013).

In addition, natural polymers can be blended with many other biomaterials such as synthetic polymers, ceramics and metal ions to improve the physiochemical and biological properties of the scaffolds. To illustrate, different types of the Alginate based biocomposite scaffolds have been noted to induce bone regeneration (Kim et al., 2015).

### 1.2.1.2. Synthetic Polymers Used in Bone Tissue Engineering

Several synthetic polymers such as polystyrene (PS), poly-L-lactic acid (PLLA), polyglycolic acid (PGA), polyvinylpyrrolidone (PVP), poly ε-caprolactone (PCL) and poly-DL-lactic-*co*-glycolic acid (PLGA) have been used to fabricate scaffolds (Rao et al., 2017). These synthetic polymers can be assessed as advantageous due to a tailored architecture, long shelf life, large scale production and low cost. To achieve success in bone-tissue engineering by using synthetic polymers, they should possess properties (Stevens et al., 2008) such as:

1) Topography of the polymeric scaffold must induce cell adhesion and growth.
2) Polymer and its degradation byproducts must not bring about inflammation or toxicity.

3) For proper diffusion and tissue growth, scaffolds should have suitable porosity percentage and appropriate pore size appropriate pore size distribution.
4) Balanced synchronization between the rate of degradation of the polymer and the newly formed bone matrix.

(PCL) is a synthetic polymer first synthesized in the 1930s from monomer, ε-caprolactone (Foggia et al., 2010). PCL is an aliphatic polyester with partial crystallinity having a melting temperature of 59-64 ˚C and a glass transition temperature about -60˚C (Foggia et al., 2010) (Figure 1.11). PCL is one of the biocompatible and nontoxic synthetic polymers according to FDA. Due to its hydrophobic character, PCL has low degradation rate. This, long degradation period of PCL creates disadvantage for bone-tissue engineering, and to overcome this problem it is usually mixed or blended with hydrophilic and fast degradable polymers. For instance, PCL can be blended with some natural polymers such as gelatin or collagen to enhance wettability and degradation rate. Furthermore, according to some researches in literature, PCL was used with bioceramics (e.g., HA) to improve bioactivity and hydrophilicity (Soundarya et al., 2017).

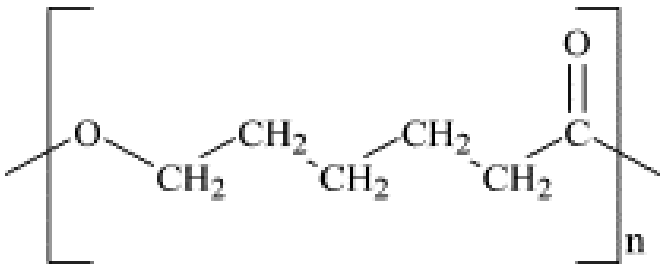


*Figure 1.11.* Chemical structure of PCL (Foggia et al., 2010).

The other synthetic polymer is PGA. Due to its degradability, it was used for biomedical applications. In some tissue engineering applications such as bone, cartilage and tooth PGA can be incorporated into scaffolds (Manoukian et al., 2019). However, PGA has some limitations such as its rapid degradation compromises its

mechanical strength and potential of undesirable inflammatory due to resulting of glycolic acid.

PLLA is another synthetic polymer. Due to excellent biocompatibility and tunable physicochemical properties PLA is used in biomedical applications. PLA is well known for controlled delivery of various therapeutic molecules such as drugs, proteins and genes. However, it has some challenges such as low encapsulation efficiency and particle heterogeneity (Jain et. al., 2019).

#### 1.2.1.3. Bioceramics

Ceramic, an inorganic material, combines metal, nonmetal or metalloid atoms. Bioactive ceramics have been used in bone-tissue engineering, due to their similarity to bone mineral components, as well as their biocompatibility, bioactivity, hydrophilicity, osteoconductivity and osteoinductivity properties (Rao et al., 2017). In 1969, Hench developed bioactive glass which has composition; $SiO_2$-CaO-$P_2O_5$-$Na_2O$. Presence of elements like silicon, calcium, and phosphorus in bioactive glass structure, provides many important properties in terms of their absorption by the cells (Niranjan et al., 2013) and bone mineralization (Price et al., 2013).

Bioceramics have also taken attention due to their topographic features and surface chemistry. They promote superior osteointegrative functions resulting in better attachment of implants. In 45S5 bioglass, atomic structure affects the alkaline ion dissolution rates creating silanol bonds (Rao et al., 2017; Soundarya et al., 2018). This induces the crystallization of ions as a layer of calcium deficient hydroxycarbonate apatite in the bone. Also, nanophase ceramics having particle sizes in nano scales, induce osteochondral tissue formation, osteogenesis and vascularisation. It is shown that the dissolution products regulate of bioglass the expression and secretion of vascular endothelial growth factor (VEGF) (Sethu et al., 2017). This means that they may enhance angiogenesis both *in vitro* and *in vivo*. In Moorthi and collaborator's studies, dissolution of silicon and calcium form the nanoceramics resulted in

osteoblast proliferation (Moorthi et al., 2014). Schematic overview about interactions between nanoceramics and osteoblasts is given in Figure 1.12.

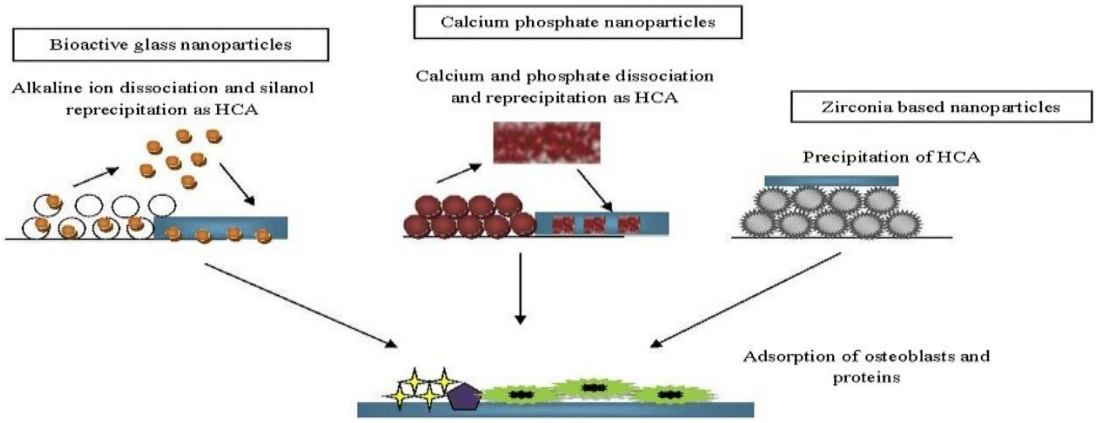


*Figure 1.12.* Relationship between nanoceramics and osteoblasts (Sethu et al., 2017).

Bioceramics are advantageous in terms of fabrication in macro, micro and nano sizes. Their scaffolds provide cell spreading and transportation of nutrients, oxygen and growth factors by tunable pore size, porosity and pore interconnection (Sethu et al., 2017). The most important factor related to bioactivity property of bioceramics is their chemical composition. As they release some ions, surface chemistry changes upon contact with body fluids thereby mineralization and attachment of proteins and/or cells take place. These series of events enhance biocompatibility and interaction with bone cells. Bioceramics can be divided into two main groups namely, calcium-phosphate (Ca-P) and calcium-silicate (Ca-Si) based bioceramics.

Ca-P's have unique properties in bone repair and regeneration because of their structural similarities to bone mineral. As mentioned before, human bone has approximately 70% HA and HA's composition is based on Ca-P system. Hence, for many years, in clinic synthetic HA and Ca-Ps such as α- and β-tricalcium phosphate (TCP) have been used for bone regeneration (Wang et al., 2014).

However, most of the Ca-P ceramics have low fracture toughness, and limited clinic applications. Hence, to overcome mechanical weaknesses and improve the bioactivity, Ca-Ps are doped with some trace elements such as Si, Zn, Sr etc (Porter et al., 2003; Maia et al., 2008; Cappucinni et al., 2009; Wang et al., 2014). These elements do not only improve mechanical problems, Ca-P based scaffolds also useful for enhancing proliferation rate, osteoconductivity and osteointegration (Table 1.2). For example, Si and Sr were shown to increase the cell expansion and osteogenic differentiation (Xing et al., 2018).

Table 1.2. *Effects of some of the trace elements on Ca-P based ceramics.*

| **Trace elements** | **Effects** | **References** |
|---|---|---|
| **Si** | Providing more rapid bone remodeling.<br>Si-HA have more osteoconductivity than pure HA. | (Porter et al., 2003) |
| **Zn** | Increased proliferation rate<br>Higher alkaline phosphatase (ALP) activity<br>Zn-HA had an enhanced osteogenesis than HA | (Pina et al., 2010)<br>(Maia et al., 2008) |
| **F** | F-HA could provide enhanced biological properties such as adhesion and proliferation | (Uysal et al., 2014) |
| **Sr** | Sr-HA showed better osteointegration property.<br>Sr-HA increased the osteoblast activity | (Capuccini et al., 2009) |

Bioactive Ca-Si based bioceramics are one of the Ca-Si based biomaterials (Wang et al., 2014), Ca-Si's have great potential for bone regeneration due to biodegradability and bioactivity. Ca and Si are dissolution products and they are beneficial for growth of bone cells.

Especially, $CaSiO_3$ based bioceramics have good potential in bone regeneration (Najafinezdah et al., 2017). For instance, $CaSiO_3$, $Ca_2SiO_4$ and $Ca_3SiO_5$ have crystal

structures and they provide apatite formation in simulated body fluid (SBF) (Wang et al., 2014). The mechanism of the bioactivity can be observed in four stages (Figure 1.13). This mechanism represents the formation of apatite layer. In the first step, release of $Ca^{2+}$ ions are occurring by exchanging $Ca^{2+}$ and $H^{+}$ ions in SBF. Due to incongruentence of $Ca^{2+}$ and $H^{+}$ ions, silanol layer (Si-O-H) is forming. Secondly, $Ca^{2+}$ ions are attracted because of the electrostatic effect to the newly formed negatively charged silanol layer. Thus, the apatite precipitation is formed. In the third stage, $Ca^{2+}$ ions attach to the Si-O surface by electrostatic attraction. In this step, also adsorption of $PO_4^{3-}/HPO_4^{2-}$ on $Ca^{2+}$ occurs. At the last step, a layer of bone-like apatite is formed on the surface of $CaSiO_3$ based ceramics (Wang et al., 2014).

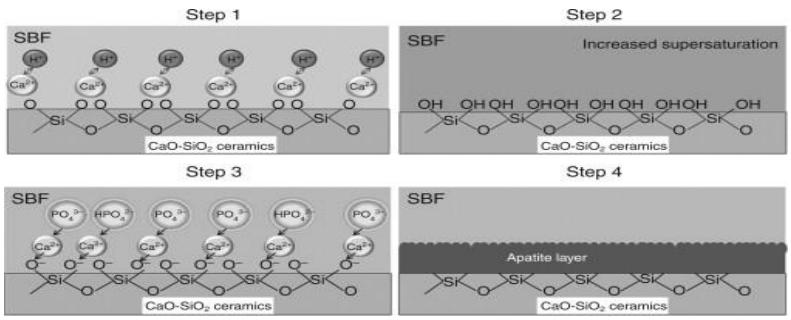


Figure 1.13. Schematic representation of the bone-like apatite formation on the $CaO\text{-}SiO_2$ bioceramics in SBF (Wang et al., 2014).

Similar to Ca-P based ceramics, even tough $CaSiO_3$ ceramics have excellent potential for bone regeneration and are close to human cortical bone in terms of bending strength. However, their mechanical properties are not good enough and their osseointegration ability is limited. To overcome this negative drawback, trace elements such as $Mg^{2+}$, $Zn^{2+}$, $Ti^{4+}$ and $Zr^{4+}$ were incorporated into Ca-Si structure (Schumacher et al., 2016).

Mg has crucial role in human metabolism. Bone tissue stores approximately half of the total physiological magnesium. In literature, related studies indicated that $Mg^{2+}$

ions had a vital role during bone remodeling and bone development. In this context, bioactive ceramics that include $Mg^{2+}$ ions have better mechanical properties, enhanced bioactivity and biocompatibility (Kharaziha et al., 2010; Ni et al., 2007). Furthermore, it was reported that these materials have induced better cell adhesion, proliferation, spreading and differentiation (Huang et al., 2009; Gu et al., 2011). Some examples of $Mg^{2+}$ ion containing bioceramics in terms of chemical formula and crystal structure are illustrated in Table 1.3.

Table 1.3. *Illustration of Mg-containing bioactive Ca-Si ceramics (Diba et al., 2014).*

| **Name** | **Chemical formula** | **Crystal System** |
|---|---|---|
| Akermanite | $Ca_2MgSi_2O_7$ | Tetragonal |
| Monticellite | $CaMgSiO_4$ | Orthorhombic |
| Diopside | $CaMgSi_2O_6$ | Monoclinic |
| Merwinite | $Ca_3Mg(SiO_4)_2$ | Monoclinic |
| Bredigite | $Ca_7Mg(SiO_4)_4$ | Orthorhombic |

*Akermanite*

In last few years, akermanite ($Ca_2MgSi_2O_7$, AKR), as a silicate bioceramic has drawn attention by researchers due to its controllable mechanical properties, corrosion rates, and bioactivity (Wu & Chang, 2004). Wu et al. synthesized AKR by sol-gel method and showed the relationship between porosity and mechanical strength. As a result, AKR was reported to cause an increase in porosity from 63.5% to 90.3% so mechanical strength increased.

In previous researches, β-TCP and AKR were compared by *in vitro* studies in terms of their bioactivity properties (Xia et al., 2011 and Sun et al., 2006). Liu et al (2016) compared bioactivity properties of akermanite and β-TCP. They seeded Human adipose-derived (hASCs) stem cells on both bioceramics. The results showed that the attachment and proliferation of hASCs on AKR ceramics were as good as on β-TCP.

Also, it was observed that cells' differentiation on AKR was better than the other (Liu et al., 2016).

There are a few *in vivo* studies about AKR ceramics. AKR and β-TCP ceramics were implanted into the bone cavities of New Zealand rabbits (Huang et al., 2009). After 16 weeks of implantation, mineral apposition rate of new bone formation in scaffolds of AKR was better than that of β-TCP. Furthermore, after 8 and 16 weeks, it was reported that material degradation rate was much more in AKR implantation than in observed for β-TCP (Huang et al., 2009).

*Diopside*

In literature, diopside ceramics were defined as the first bioactive ceramics in type of Mg-including silicate ceramics (Kobayashi et al., 1997). Diopside can be synthesized by different methods such as solid-state (Nonami & Tsutsumi, 1999) and coprecipitation (Iwata et al., 2004) techniques. However, sol-gel method is more advantageous than the others due to lower crystallization temperature of synthesis (Nonami & Tsutsumi, 1999).

Mechanical properties of the diopside were also studied in two relevant researches. According to results, mechanical properties of diopside were higher than those of HA. Density of HA is 3.16 g/cm$^3$, whereas density of diopside is 3.20 g/cm$^3$. Bending strength of diopside is 300 MPa, fracture toughness is 3.5 MPa m1/2 and Young's modulus is 170 GPa (Wu et al., 2010).

According to Kobayashi et al. MC3T3-E1 cells cultured on diopside discs had higher ALP activity and differentiation. In addition, they induced mineralization in the environment and provided adhesion of the fibroblasts L-929 (Kobayashi et al., 1997).

Similar to akermanite, there are few *in vivo* experiments for diopside. For example, Kobayashi et al. studied diopside with white Japanese rabbits. It was shown that diopside attached to rabbit bone and it was degraded and replaced by newly formed bone after 20 weeks (Kobayashi et al., 1997; Diba et al., 2014).

*Bredigite*

Bredigite is another Ca-Si ceramic which has orthorhombic crystal system (Table 1.3). In literature, there are many preparation methods for bredigite such as sol-gel (Wu et al., 2005), mechanical activation annealing (Tavangarian & Emadi, 2011) and combustion (Huang & Chang, 2008). However, the most advantageous technique is a simple solution combustion method due to preparation at lower temperature and obtaining pure nanocrystalline bredigite powders (Huang & Chang, 2008).

There are a few mechanical studies about bredigite in literature. According to Wu et al., bredigite synthesized by sol-gel method had a bending strength of 156 MPa, fracture toughness of 1.57 MPa m1/2, and Young modulus of 43 GPa (Wu et al., 2005).

Zhai et al. studied bredigite by *in vitro* studies. They studied the effect of bredigite ceramics on the osteogenic differentiation of hBMSCs and the angiogenesis by human aortic endothelial cells (HAECs) was also investigated. In this study, results showed that bredigite had more potential with respect to osteogenic and angiogenic properties than akermanite and diopside (Zhai et al., 2013).

*Monticellite*

Monticellite is another example of Mg based bioceramic. It has high biocompatibility, bioactivity and degradation rate (Diba et al., 2014 and Bakhsheshi-Rad et al., 2019a). Monticellite was also synthesized by sol-gel method (Chen et al., 2007).

Chen et al., compared the mechanical properties of monticellite and HA. It was shown that Young's modulus of monticellite was closer to that of human cortical bone (7-30 GPa), bending strength of monticellite was higher than that of HA and fracture toughness of monticellite (1.63 MPa m1/2) was higher than that of HA (0.86 MPa m1/2) (Chen et al., 2007).

*In vitro* studies with mouse osteoblast-like cells, G292 showed that monticellite was cytocompatible (Kalantari et al., 2018). According to Diba's report, osteoblasts can

adhere and spread over monticellite's surface, thus, it promoted osteoblast cells' growth (Diba et al., 2014).

*Merwinite*

In 2008, merwinite was firstly synthesized by sol-gel method by Ou's group (Ou et al. 2008). It was found that Young's modulus, fracture toughness and bending strength were approximately 31 GPa, 1.72 MPa m1/2, and 151 MPa, respectively (Ou et al., 2008).

*In vitro* cell culture tests showed that merwinite surface provided good environment for osteoblasts adherence and spreading (Diba et al., 2014). In addition, according to Kalantari's results, bioactivity analysis of merwinite in SBF confirmed the growth of apatite on the surface of merwinite ceramics (Kalantari et al., 2018). By *in vivo* experiments, merwinite was used in rat femoral defects (Diba et al., 2014). Merwinite implantation showed a higher biodegradation rate than HA ceramics (Hafezi et al., 2013).

### 1.2.2. Composites

A composite is composed of at least two different materials that have different characteristics and are separated by a distinguishable interface (Rahaman et al., 2017). Composite materials promote an opportunity to produce a new material which shows synergistic characteristics of the individual materials (Callister & William D., 2007). Therefore, to overcome some negative drawbacks and limitations on properties of bone-tissue engineering scaffolds, various materials such as bioceramics and synthetic polymers are combined to obtain composite structures.

As mentioned before, to achieve success in bone-tissue engineering in terms of bone regeneration, scaffolds must have some properties such as biodegradability, osteoconductivity, osteoinductivity, flexibility, mechanical features compatible with the bone, 3D physical shapes, interconnective and porous structures (Soundarya et al., 2018b). Combination of synthetic polymers and bioceramics provides many

advantages in bone-tissue engineering such as improved degradation rate, ion release and better mechanical properties (Song et al., 2007).

### 1.2.3. Effect of Silicon and Magnesium Ion on Immune Response and Angiogenesis

It is a fact that angiogenesis and immune response are two very important issues for bone tissue engineering. In literature, researchers compared Mg and Si containing bioceramics such as AKR, bredigite, nagelschmiditte and diopside for bone tissue engineering. Huang et al. (2018) compared akermanite, nagelschmiditte ($Ca_7Si_2P_2O_{16}$) and β-TCP. Firstly, they detected that ions such as $Mg^{2+}$, $Si^{4+}$ in akermanite extract and $Ca^{2+}$ and $Si^{4+}$ in nagelschmiditte are higher than those in β-TCP extracts. In this study, response of system immune of minerals was found different from each other; number of macrophages on AKR and nagelschmiditte was less than β-TCP (Huang et al., 2018). In another study, Zhai et al. compared AKR, bredigite diopside and TCP (Zhai et al., 2013). According to their results, bredigite had the highest angiogenic potential, whereas diopside showed the lowest angiogenic potential due to less amount of Si release. In addition, they found that AKR ceramics induce angiogenesis and bone regeneration much more than β-TCP ceramics *in vitro*. They also investigated alkaline phosphatase, an enzyme use as an early marker of osteogenic differention activity, (ALP) of hBMSC exposed to these ceramic extracts and detected that AKR, bredigite and diopside showed higher ALP activity than β-TCP (Zhai et al., 2013).

### 1.2.4. Fabrication Processes of Scaffods

Scaffolds in bone-tissue engineering must satisfy following criteria (Wubneh et al., 2018):

• Surface permeability to induce transfer of biological fluids at the boundary.

• In order to provide cell attachment and osteoconductivity, appropriate surface roughness is needed.

To decrease the risks of local toxicity and also have inflammatory response at minimum level, scaffolds must be biocompatible.

• Scaffolds must be biodegradable and byproducts removal should occur with physiological metabolic processes

• Porosity and internal architecture are necessary for the scaffold invasion by cells and for deposition of ECM.

• Mechanical properties of scaffolds and tissues must be matched.

There are many fabrication techniques of bone-tissue engineering scaffolds such as electrospinning, sol-gel method, solvent casting, melt molding, compression molding, 3D printing, etc.

### 1.2.4.1. Elecrospinning

Electrospinning is a technique of converting a viscoelastic solution into nanofibers by using a high electrostatic force. A syringe is filled by a polymeric solution which is pumped at a slow flow rate by the syringe pump (Figure 1.14) (Balagangadharan et al., 2017).

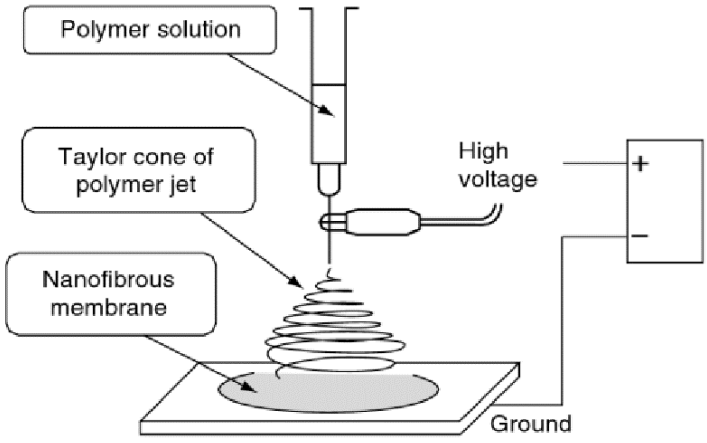


*Figure 1.14.* A schematic representation of electrospinning technique (Morais, 2011).

By applying high voltage electricity to the droplet of liquid solution at the tip, a cone shape is formed, named as Taylor cone. When applied voltage is enough to overcome the surface forces of the polymer solution this narrow jet of polymer solution moves toward the collector (Balagangadharan et al., 2017; Soundarya et al., 2018). While the liquid jet goes to the collector, the solvent evaporates from the fiber and solid fiber is deposited on the collector. In this method, four main parameters can be adjusted for obtaining proper electrospun structures (Balagangadharan et al., 2017):

• Flow rate of the polymer solution.

• Concentration of the polymer solution.

• Voltage applied to the needle.

• The distance between the needle and the collector.

The disadvantage of classical electrospinning is that collected scaffolds are mostly in 2D structure, thus lacking suitable pore size to support cellular invasion (Dalton et al., 2010). Due to this, wet electrospinning became an alternative method where fibers are collected incoagulation bath contains nonsolvent of the polymer (e.g., ethanol) and this environment creates 3D scaffold with larger diameters of fibers (Atila et al., 2015) due to not accumulation of fibers on each other as in the case of classical electrospinning. Illustration of a wet electrospinning system is shown in Figure 1.15.

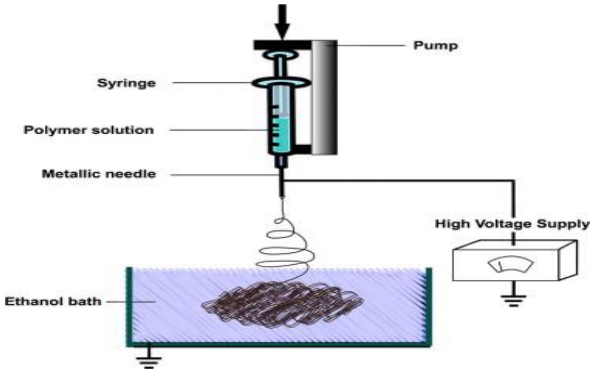


*Figure 1.15.* An illustration for wet electrospinning system (Yang et al., 2013).

### 1.2.4.2. Sol-Gel Method

Sol gel is a wet chemical process that includes the formation of an inorganic colloidal suspension (sol) and gelation of the sol. The sol in a continuous liquid is named as gel and at the end of the process, 3D structure is obtained (Asmatulu et al., 2012). Sol-gel method produces porous and ordered powder. The gel's composition includes discrete particles or polymers (Soundarya et al., 2018). Metal alkoxide and chlorides are widely used in sol-gel. Mixing, casting and gelation are its main stages (Figure 1.16) (Asmatulu et al., 2012; Soundarya et al., 2018).

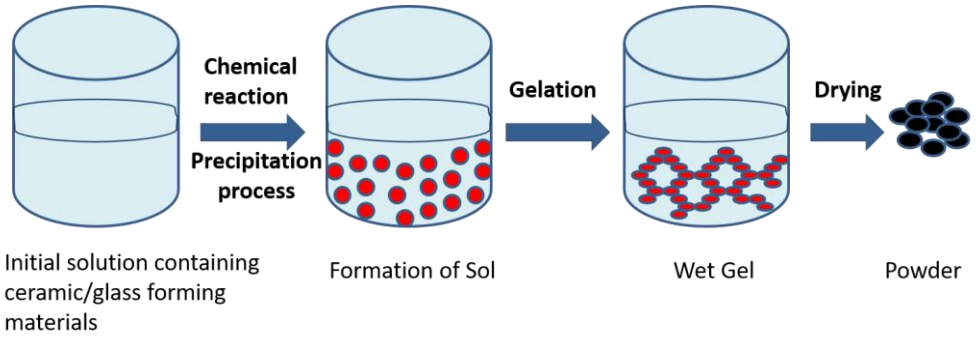


*Figure 1.16.* A schematic representation of the sol-gel process.

In the mixing step, a colloidal solution is formed by mechanical stirring of colloidal substances in a solvent. Metal alkoxides react with the solvent and undergo to hydrolysis and polycondensation reactions. In casting stage, due to low viscosity of the sol, formation of the cast into mold is easy. In gelation step, 3D structures begin to form from colloidal particles because of agglomeration of the colloidal particles. After gelation, aging, drying and dehydration steps are applied to create solidifying and porous material. At the end of the densification, gel is exposed to temperature to solidify. Sol-gel is an applicable technique especially for bioceramics and bioglasses due to economic feasibility and the low temperature processing that induce control of the products in terms of structure (Hench & West, 1990; Soundarya et al., 2018b).

### 1.3. Aim of the Study

In this thesis, it was aimed to develop bioceramic/polymer composites with new compositions and investigate their properties as a candidate for BTE scaffold. For this aim, composites of PCL with minerals (Bioceramics), hydroxyapatite (HA), carbonated hydroxypatite (CHA), Akermanite (AKR) and various combinations of these minerals were prepared by wet electrospinning method. In order to achieve correct composite structure, first, successful synthesis of the minerals and their characterizations were done. Then mineral combinations at specific ratios were characterized (e.g. bioactivity, degradation etc.) were for selection of suitable groups to be used in composite studies.

# CHAPTER 2

# MATERIALS AND METHODS

## 2.1. Materials

Materials used for synthesis of hydroxyapatite (HA), carbonated hydroxyapatite (CHA) and akermanite (AKR): Calcium nitrate tetrahydrate ($Ca(NO_3)_2 \cdot 4H_2O$), di-ammonium hydrogenphosphate ($(NH_4)_2HPO_4$), tetraethyl orthosilicate ($(C_2H_5O)_4Si$, TEOS), magnesium nitrate hexahydrate ($Mg(NO_3)_2 \cdot 6H_2O$), ammonium bicarbonate ($NH_4HCO_3$), nitric acid ($HNO_3$) were purchased from Merck (USA).

Sodium chloride (NaCl), sodium bicarbonate ($NaHCO_3$), potassium chloride (KCl), dipotassium hydrogen phosphate trihydrate ($K_2HPO_4 \cdot 3H_2O$), magnesium chloride hexahydrate ($MgCl_2 \cdot 6H_2O$), 1.0M hydrochloric acid (HCl), calcium chloride ($CaCl_2$), sodium sulfate ($Na_2SO_4$), TRIS, disodium hydrogen phosphate dihydrate ($Na_2HPO_4 \cdot 2H_2O$) and dipotassium hydrogen phosphate ($K_2HPO_4$) were obtained from Merck (USA) and were used to prepare simulated body fluid (SBF), and phosphate buffered saline (PBS).

Materials used for cell culture studies: Saos-2 cell line (USA), high glucose Dulbecco's modified Eagle medium (DMEM) (Merck, Germany), fetal bovine serum (FBS) (Biological Industries, USA), penicillin/streptomycin (Biological Industries, USA), Alamar Blue (Invitrogen, USA), cupric sulfate pentahydrate ($CuSO_4 \cdot 5H_2O$) (Sigma, USA), bicinchoninic acid solution (Sigma, USA), *p*- nitrophenyl phosphate (pNPP) (Invitrogen, USA), ascorbic acid (Sigma, USA), β-glycerophosphate (Sigma, USA), magnesium chloride solution ($MgCl_2$) and dexamethasone were used. Also, HCl (Merck, USA), 1 N NaOH, paraformaldehyde powder (Sigma, USA) and hexamethyldisilazane (Sigma, USA) were used for fixation of cells.

## 2.2. Methods

### 2.2.1. Synthesis of AKR

AKR was synthesized by sol-gel method (Wu & Chang, 2004). Firstly, 30 mL 2N $HNO_3$ solution was prepared. Then, 30 mL TEOS was added to the mixture slowly at room temperature. After adding TEOS, solution was stirred for 30 minutes with magnetic stirrer. After that, 0.0585 mole of $Mg(NO_3)_2 \cdot 6H_2O$ and 0.1270 mole of $Ca(NO_3)_2 \cdot 4H_2O$ were added to the solution and this mixture was stirred for 5 h at room temperature (Figure 2.1a). After mixing, a gel form was obtained (Figure 2.1b) and it was dried in two steps; at 60˚C for 24 h and at 120˚C for 48 h. Finally, dried powder was obtained (Figure 2.1c). It was crushed with mortar and AKR powders were sintered at 900, 1100 and 1300˚C (Figure 2.1d).

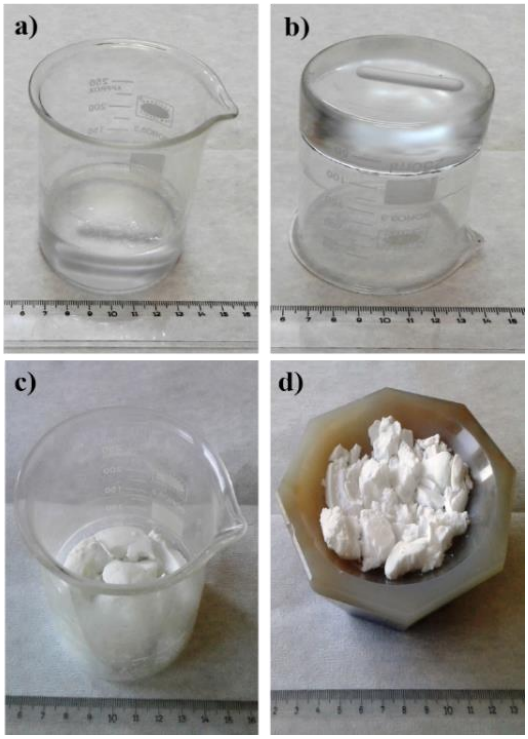


*Figure 2.1*. Experimental photographs of synthesized AKR (by Sol-Gel method): a- b) solution and gel forms, c- d) powder forms before and after sintering respectively.

### 2.2.2. Synthesis of HA

HA was synthesized by microwave irradiation method (Farzadi et al., 2011). Firstly, 0.2 mole of $Ca(NO_3)_2 \bullet 4H_2O$ (calcium source) and 0.12 mole of $(NH_4)_2HPO_4$ (phosphate source) were separately dissolved in 200 mL distilled water. After that, phosphate solution was titrated to solution containing calcium source (Figure 2.2). During the titration, ammonia solution was added to the mixture slowly. At the end of the titration, a white mixture was obtained and stirred for 30 min at room temperature. Then, the mixture was exposed to microwave irradiation at 800 W for 15 min. After that, the mixture was filtrated and rinsed with distilled water for neutralization. Finally, filtrate was dried at 80˚C overnight. Dry HA was crushed with mortar and powders were sintered at 1100˚C for 1h.


*Figure 2.2.* Photograph of experimental setup for synthesis of HA showing titration of calcium solution with phosphate solution.

### 2.2.3. Synthesis of CHA

CHA was produced with nanoemulsion method (Ezekiel et al., 2018). Firstly, 0.06 mole of $(NH_4)_2HPO_4$ and 0.04 mole of $NH_4HCO_3$ were dissolved separately in 60 mL

and 40 mL deionized water, respectively, and stirred for 15 min. After that, two solutions were mixed and stirred for 15 min. During this stage, 0.1 mole of $Ca(NO_3)_2 \bullet 4H_2O$ was dissolved in 100 mL acetone. Then, this solution was poured into former solution and stirred. Synthesis occurred in basic environment (pH 11) which was formed by 2.0 M NaOH solution. At the final stage, a white cake was obtained. In order to eliminate impurities it was washed 3 times with 1 L deionized water. Then, CHA was dried in an oven at 90˚C for 24 h. Dried CHA was crushed with mortar. CHA powders were characterized by XRD and FTIR analyses.

### 2.2.4. Characterizations of AKR, HA and CHA

AKR, HA and CHA were characterized with X-ray diffraction (XRD) and Fourier transform infrared (FTIR). XRD was applied for studying crystal structure of the synthesized ceramics and FTIR was to determine of functional groups of materials.

XRD analysis was performed with a diffractometer (Rigaku Ultima-IV, Japan) with Cu-Kα radiation at 40 kV and 30 mA. The scan range was between 10 and 90˚ in 2θ. The ratio of duration time/scan was 1 deg/min and the ratio of step/sampling step was 0.02 deg. The phases present in the sample were determined by using the database of International Centre for Diffraction Data (ICDD).

For FTIR analysis, the system consisting of a spectrometer and a microscope (Bruker IFS 66/S an Hyperion 1000, Germany) was used. The analysis was carried out between 4000-400 $cm^{-1}$ wavenumbers, with a resolution of 4 $cm^{-1}$, with a total of 50 scans per sample. The samples were crushed with pestle and mortar and mixed with KBr at a ratio of 1:10 to measure. Spectra of samples were corrected for background and atmosphere.

### 2.2.5. Preparation and Characterization of HA:AKR and CHA:AKR Composites

HA:AKR composites were prepared at different weight proportions (Table 2.1). To prepare a homogenous mixture, ball milling was used. Firstly, HA and AKR powders

were crushed separately for 1h with zirconium balls (The mass ratio between balls and powders were 30:1). Then, HA:AKR mixtures were crushed by ball milling for 1 h. Composites were characterized by XRD and particle size analyses. Details of XRD analysis are given above in Section 2.2.4. CHA:AKR (90CHA10AKR) composites were prepared according to the same protocol. Furthermore, to observe the effect of the milling time on particle size, particle size analysis was done. Analysis was carried out with pure AKR powders. There were two AKR groups: one of them was milled for 1 h and the other was milled for 10h. At the end of the millings, particles were dispersed in deionized water and then particle sizes were measured by particle size analysis at the METU central Lab (Malvern Mastersizer 2000) according to Mie theory. The Mie Theory depends on the breaking and permeability of the light around the grain size in the medium.

Table 2.1. *HA:AKR and CHA:AKR composites prepared at different weight ratios*.

| **Compound name** | **Weight ratio of HA (wt %)** | **Weight ratio of CHA (wt %)** | **Weight ratio of AKR (wt %)** |
|---|---|---|---|
| 100HA | 100 | - | - |
| 100CHA | - | 100 | - |
| 100AKR | - | - | 100 |
| 66HA33AKR | 66.5 | - | 33.5 |
| 33HA66AKR | 33.5 | 66.5 | - |
| 50HA50AKR | 50 | - | 50 |
| 90HA10AKR | 90 | - | 10 |
| 90CHA10AKR | - | 90 | 10 |

#### 2.2.5.1. Bioactivity and Biodegradability Tests of Composites

After preparation of composites of HA:AKR by ball milling, about 0.25 g of composite powder was weighed and discs (n=3) were prepared by using cold compression method. After that, bioactivity and biodegradability tests were conducted. To determine apatite layer formation on the discs' surfaces, SEM analysis was applied. Before the analysis, samples were coated with gold (Au) and palladium

(Pd). The sputter coated disks were observed by SEM (QUANTA 400F Field Emission SEM). For analyzing bioactivity of composites, simulated body fluid SBF was prepared according to modified Kokubo's solution (Kokubo et al., 1990). Necessary amounts of NaCl, $NaHCO_3$, KCl, $K_2HPO_4 \cdot 3H_2O$, $MgCl_2 \cdot 6H_2O$, $CaCl_2$, $Na_2SO_4$ were orderly dissolved in 1000 mL distilled water (Table 2.2). TRIS and 1.0 M HCl were used to adjust pH. At the end of the preparation, SBF had pH 7.40. Addition of hygroscopic chemicals such as KCl, $K_2HPO_4 \cdot 3H_2O$, $MgCl_2 \cdot 6H_2O$, $CaCl_2$, $Na_2SO_4$ into SBF should be as fast as possible, because they can absorb moisture in the air.

Table 2.2. *Composition of SBF solution (Kokubo et al., 1990).*

| **Chemicals** | **Amounts** | **Purity (%)** | **Molecular weight** |
|---|---|---|---|
| NaCl | 8.035 g | 99.5 | 58.443 |
| $NaHCO_3$ | 0.355 g | 99.5 | 84.006 |
| KCl | 0.225 g | 99.5 | 74.551 |
| $K_2HPO_4 \cdot 3H_2O$ | 0.231 g | 99.0 | 228.222 |
| $MgCl_2 \cdot 6H_2O$ | 0.311 g | 98.0 | 203.304 |
| HCl (1.0M) | 39.00 mL | - | - |
| $CaCl_2$ | 0.292 g | 95.0 | 110.984 |
| $Na_2SO_4$ | 0.072 g | 99.0 | 142.042 |
| TRIS | 6.118 g | 99.0 | 121.135 |

To prepare phosphate buffered saline (PBS) for degradation studies, necessary amounts of NaCl, KCl, $Na_2HPO_4$ and $KH_2PO_4$ were dissolved in 1000 mL of distilled water (Table 2.3). Firstly, chemicals were dissolved in 800 mL of water. Then, the total volume was adjusted to 1000 mL with deionized water. The final pH value was adjusted to 7.40.

Table 2.3. *Preparation of PBS solution.*

| **Chemicals** | **Amounts (g)** |
|---|---|
| NaCl | 8.00 |
| KCl | 0.20 |
| $Na_2HPO_4$ | 1.44 |
| $KH_2PO_4$ | 0.24 |

For bioactivity; prepared HA:AKR composite discs were incubated in 10 mL of SBF solution at 37 °C for 1, 7 and 14 days. At the end of each period, disks were dried and weighed. In addition, SEM was used to observe apatite layer formation. In addition, EDX analysis was done to determine Ca/P ratio on the disks' surface. Same SBF protocol was separately applied for HA, CHA and AKR.

For degradation analysis; prepared disks of HA:AKR were awaited in 10 mL of PBS solution at 37˚C for 1, 7 and 14 days. At the end of each period, wet and dried disks were weighed to determine swelling ratio (SR) and weight loss. To calculate SR, equation 1 was used ($w_t$: Weight of disk at immersion time, $w_i$: Initial weight of disk) (Chen et al., 2018).

$$SR = \frac{(Wt - Wi)}{Wi} \; x \; 100 \qquad (1)$$

Also, the pH change of environment was monitored. Same PBS protocol was separately applied for HA, CHA and AKR.

### 2.2.5.2. Mechanical Tests of Bioceramics

HA, AKR, CHA, 90HA10AKR and 90CHA10AKR discs (3 discs for each group) with a diameter of approximately 12 mm and a thickness about 3 mm were used. Discs were produced from ceramics powder by cold press technique. In this method, the maximum tensile stress is formed across the flat surface diameters of discs.

Universal Instron Compression/Tension machine (METU, Turkey) was used for mechanical testing. The speed of the machine was 3 mm/min during the test. The

following formula was used to calculate the diametral tensile strength of the sample (Kamst et al., 1999; Thomas et al., 1980):

$$S = \frac{2F}{(\pi \bullet D \bullet t)} \quad (2)$$

where:

F: failure force; D: diameter of sample; t: thickness of sample.

For all ceramic groups, load (N) vs extension (mm) graphs were drawn (Appendix A-E).

### 2.2.6. Preparation of HA/AKR/CHA Loaded PCL Scaffolds with Electrospinning

Concentrations of PCL such as 10%, 15% and 20% were prepared in acetone. During dissolution process, 40-50˚C was applied by magnetic stirrer with heater. After dissolution, a wet electrospinning system was used and fibers were collected in ethanol bath which was stabilized on a rotational collector (Gozeler Elektronik, Turkey) at a distance of 10 cm (Figure 2.3). As seen in Figure 2.3, polymer solution was pumped by NE-1000 syringe pump (New Era Pump Systems, USA) at 4 mL/h flow rate and under 10.3 kV which was supplied using high voltage source (ES30, Gamma High Voltage Research, Inc., USA). Obtained fibers were lyophilized with freeze dryer (Labconco Corporation, USA) about 1 day. SEM examinations showed that 20% PCL/acetone solution has the best morphology of the fibers for spinning. For mineral loaded scaffolds, 20% PCL/acetone solutions were prepared with addition of HA, CHA, HA/AKR and CHA/AKR. Mineral percentages were 5%, 8% and 10% according to amount of PCL solution. SEM results revealed that 10% mineral was the best addition. While all spinning parameters were same for HA, CHA and HA/AKR, flow rate was different for CHA/AKR composite. Adjusted parameters for electrospinning are shown in Table 2.4.

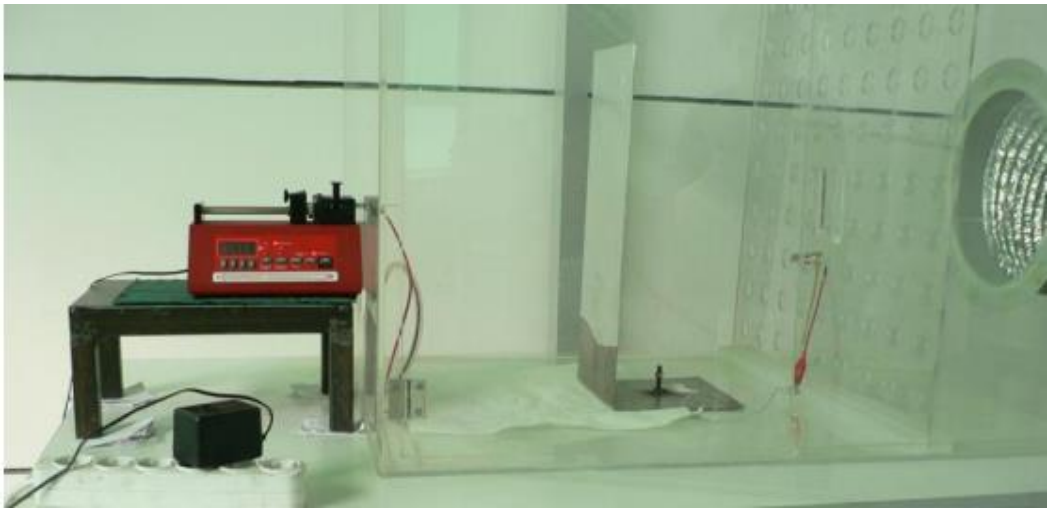

*Figure 2.3.* Electrospinning set-up.

Table 2.4. *Parameters of wet spinning for 20% PCL/acetone, HA, CHA, HA/AKR and CHA/AKR in terms of flow rate, voltage and the distance between needle and ethanol bath*.

| **Samples** | **Flow rate (mL/h)** | **Voltage (kV)** | **Distance between needle and ethanol bath (cm)** |
|---|---|---|---|
| 20% PCL/acetone | 4 | 10.3 | 10 |
| PCL-10% HA | 4 | 10.3 | 10 |
| PCL-10% CHA | 4 | 10.3 | 10 |
| PCL-10% 90HA10AKR | 4 | 10.3 | 10 |
| PCL-10% 90CHA10AKR | 5 | 10.3 | 10 |

### 2.2.6.1. Characterizations of Scaffolds

Mineral loaded scaffolds were exposed to SBF (Table 2.2) and PBS (Table 2.3) solutions to determine mineralization and degradation, respectively. Approximately 0.005 g of scaffolds (n=3) was awaited (in 15 mL of falcon) in water bath for 1, 7 and 14 days at 37˚C for both analyses. Change in weights and pH were monitored at all point of times as described above. To observe apatite layer formation on the mineral

loaded fibers, SEM analysis was applied. To determine elemental analyses EDX analysis was applied.

### 2.2.7. Cell Culture Studies

Cell culture studies were performed with Saos-2 cell line (ATCC, USA). Culture medium for cell growth was prepared with DMEM, 10% FBS, 1% penicillin/streptomycin. Cells were maintained in carbon dioxide incubator (Shel Lab, USA) at 37ºC. For the cell culture study, scaffolds were cut small pieces to fit 48-well plate. Before placing to well, sterilization steps were done. Firstly, the scaffolds were incubated in ethanol for 2 h. Secondly, UV treatment was applied for 30 min to each surface. Initially, $2 \times 10^4$ cells/scaffold were seeded.

Alamar Blue assay was applied for 1, 4 and 7 days to determine cell viability and proliferation on scaffolds (n=4). In addition to scaffolds groups, there were also control (cells on TCPS) and blank groups (scaffolds without cells). Alamar reagent DMEM (10% v/v) was prepared with DMEM without phenol red (10%, v/v). PBS was used to wash scaffolds for removing the medium. Then, 500 µL Alamar solution was added to each well. Scaffolds were put into incubator in 37ºC for 6 h in dark. After that, Alamar solutions were separately put to new 48-well plate. Reductions of separated Alamar solutions were read at 570 and 600 nm wavelengths. Then, samples were washed with PBS for removing Alamar dye. At last, the process was returned back to normal growth conditions with growth medium till the next time point. Also, often the growth medium of each plate was changed.

Percentage reduction of Alamar Blue can be calculated with formula;

$$\frac{(O2\times A1)-(O1\times A2)}{(R2\times N2)-(R2\times N1)} \times 100 \qquad (3)$$

Where;

$O_1$; molar extinction coefficient (E) of oxidized alamarBlue (Blue) at 570 nm

$O_2$; E of oxidized alamarBlue (Blue) at 600 nm

$R_1$; E of reduced alamarBlue (Red) at 570 nm

$R_2$; E of reduced alamarBlue at 600 nm

$A_1$; absorbance of test wells at 570 nm

$A_2$; absorbance of test wells at 600 nm

$N_1$; absorbance of negative control well (media plus alamarBlue but no cells) at 570 nm

$N_2$; absorbance of negative control well (media plus alamarBlue but no cells) at 600 nm

Alkaline phosphatase (ALP) activity experiments were applied for studying osteogenic activity of Saos-2 cells seeded the developed scaffolds. Firstly, osteogenic differentiation medium was prepared with DMEM including 10% FBS, 1% penicillin/streptomycin, 50 µg/mL ascorbic acid, 10 mM β-glycerophosphate and $10^{-8}$ M dexamethasone in ethanol. 0.005 g of scaffolds (n=3) seeded with cells were incubated for 7 and 14 days in this media. Also, there were control groups for each scaffolds group. After each incubation period, ALP assay was applied. As a summary, cells on scaffolds were lysed by two freezing and thawing cycles at -80ºC and 37ºC with 15 min incubation for all temperature. Lysates were put into 500 µL PBS. After that, they were transferred (25 µL) into 96-well plate with 75 µL pNPP solution. In this part, to increase reaction speed $MgCl_2$ solution was used. Plate containing scaffolds was incubated at 37ºC for 1 h. Then, absorbance was measured at 405 nm by using Elisa plate reader (Spectramax ID3, San Jose, USA). To detect ALP activity, a calibration curve was built with different concentration p-nitrophenol (Appendix F).

To observe cell adhesion and spreading on the scaffolds, SEM analysis was applied. For fixation of cells parafomaldehyde solution (4%) was used. Firstly, 40 g of paraformaldehyde was added into heated PBS (60˚C). To obtain clear solution, 1 N NaOH was added slowly. Finally, pH of solution was adjusted to 6.9 by using dilute

HCl. After fixation of cells for both hexamethyldisilazane was added on the scaffolds. Then, scaffolds with cells were analyzed with SEM.

### 2.2.8. Statistical Analysis

Statistical analyses were done by using Tukey's Multiple Comparison Test for the post hoc pairwise comparisons (SPSS 22 Software Program, USA). Differences were accepted at statistically significant at $p<0.05$. The results are expressed as mean ± standard deviation.

# CHAPTER 3

# RESULTS AND DISCUSSIONS

## 3.1. Characterization Results of Synthesized Minerals: AKR, HA, CHA

After synthesis, AKR was analyzed for verification of structural characteristics. For this purpose, firstly, XRD Spectrum of AKR was investigated after sintering at different temperatures; 900, 1100 and 1300˚C. According to XRD results, besides AKR, other ceramic phases such as merwinite and diopside were also present (Figure 3.1). Specifically, at 2θ=35˚ merwinite ((2, 1, -3), Joint Committee on Powder Diffraction Standards No, JCPDS No: 01-074-0382) and diopside ((0, 0, 2), JCPDS No: 01-071-1494) were determined at 900˚C; at 2θ=32˚ akermanite ((2, 2, 0), JCPDS No: 00-035-0592) and merwinite ((4, 0, -2), JCPDS No: 00-035-0592) were observed at 1100˚C. However, quantitative analysis confirmed that AKR was more dominant at 1300˚C than the other sintering temperatures. In other words, XRD study of AKR at different sintering temperatures showed that 1300˚C was the optimum sintering temperature due to presence of characteristic peak (Wu & Chang, 2004)) of AKR (2θ=31˚, (2, 1, 1), JCPDS No: 01-079-2425, Figure 3.1).

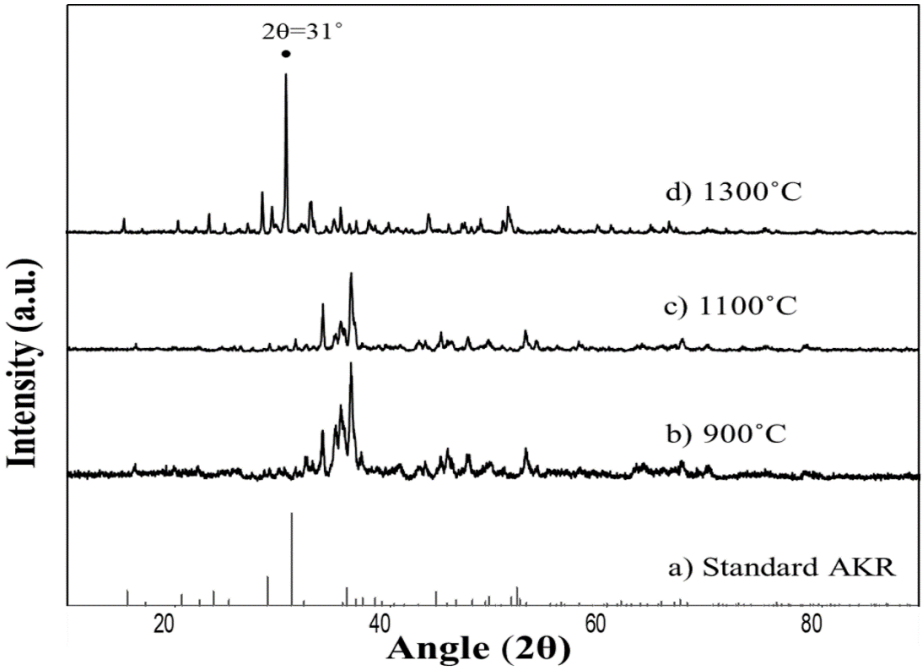


*Figure 3.1.* XRD Spectra of AKR samples: a) standard AKR (JCPDS no: 01-079-2425), sintered AKR; b) at 900˚C, c) at 1100˚C, d) at 1300˚C.

In the FT-IR spectra of AKR, characteristic bending modes were observed (Figure 3.2). Absorption bands at 400 $cm^{-1}$ and at 471 $cm^{-1}$ can be observed due to vibrations of O-Ca-O and O-Mg-O, respectively. The absorption bands corresponding to O-Si-O were seen at 635 and at 680 $cm^{-1}$, and for the Ca=O group, at 586 $cm^{-1}$ (Najafinezhad et al., 2017). Also, due to the stretching modes of Si-O groups, the absorption bands are observed at 848, 924 and 971 $cm^{-1}$ (Chen et al., 2014).

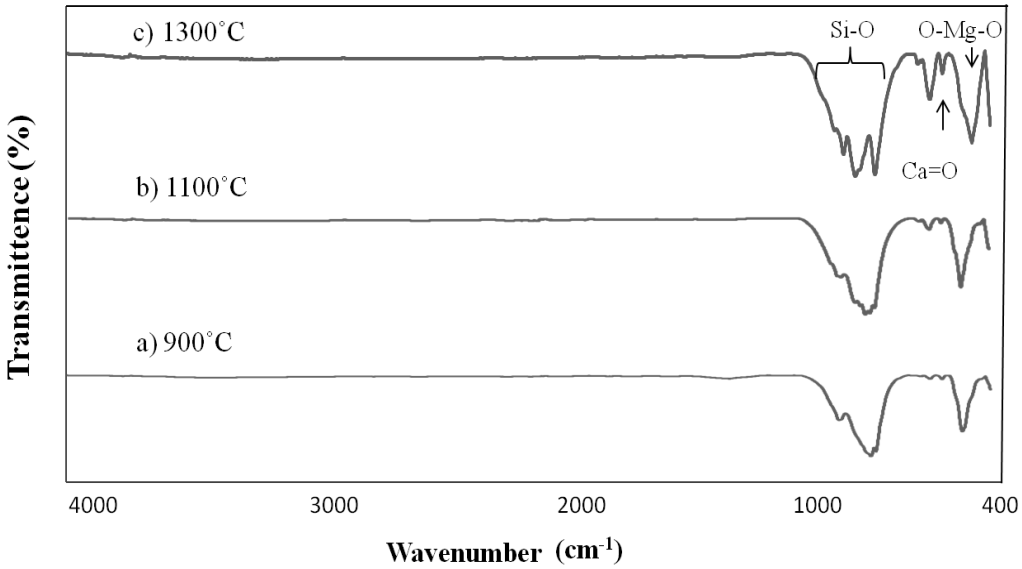


*Figure 3.2.* FT-IR spectra of AKR samples sintered at different temperatures: a) 900˚C, b) 1100˚C, c) 1300˚C.

Synthesized HA was also characterized by XRD analysis for structural properties of the mineral. Analysis was applied to HA samples that were sintered at 1100˚C; both before and after the ball milling for 1 hour (Figure 3.3). XRD showed that HA was successfully synthesized; however, specific peaks of tricalcium phosphate ($Ca_3(PO_4)_2$) having small intensities were also observed.

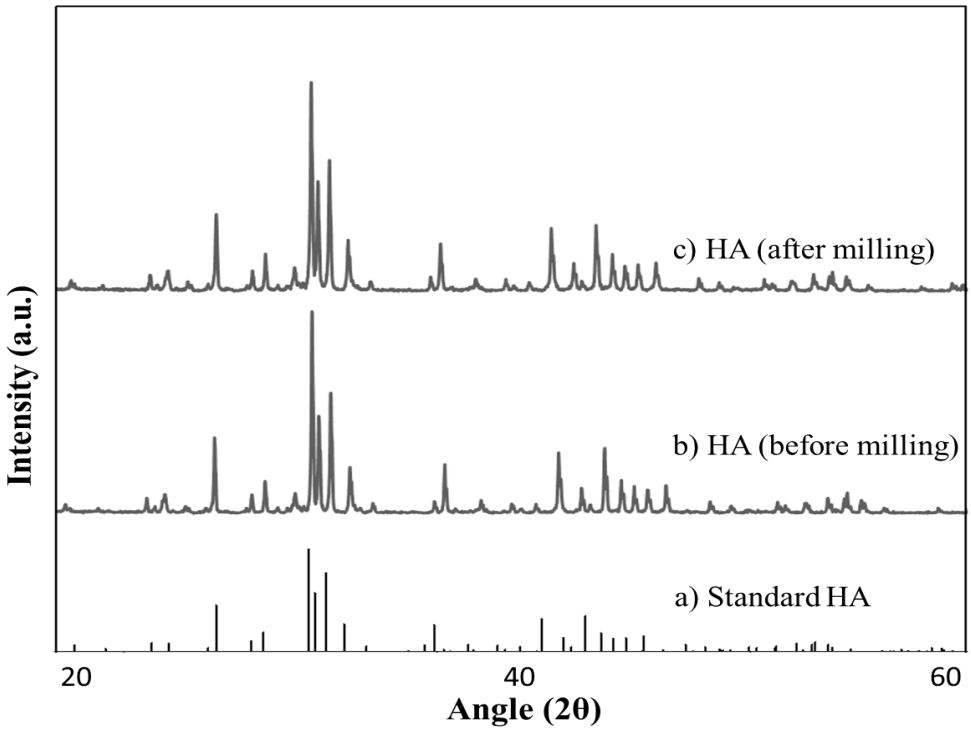


*Figure 3.3.* XRD Spectra of HA after sintering at 1100 ˚C: a) Standard HA (International center for Diffraction Data, ICDD: 896439), b) HA (before ball milling), c) HA (after ball milling).

In FTIR spectrum of HA, typical vibrations of P-O were observed at 961, 1023 and 1087 $cm^{-1}$. Also, O-P-O absorption bands were observed at 561, 598 and O-H vibrations were seen at 629 $cm^{-1}$ (Nga et al., 2012) (Figure 3.4). While the band at 473 corresponds to $v_2$ mode of $(PO_4)^{3-}$, the bands at 1087, 1023 and 961 $cm^{-1}$ correspond to $v_3$, $v_3$ and $v_1$ vibrational modes of $(PO_4)^{3-}$ (Uysal et al., 2014). Hence, these vibration modes showed that HA was synthesized successfully with microwave irradiation method. As seen in Figure 3.3. there is no any difference between before milling and after milling. This result is normal because milling process is a physical process. Thus, it cannot lead to any chemical change in the HA structure.

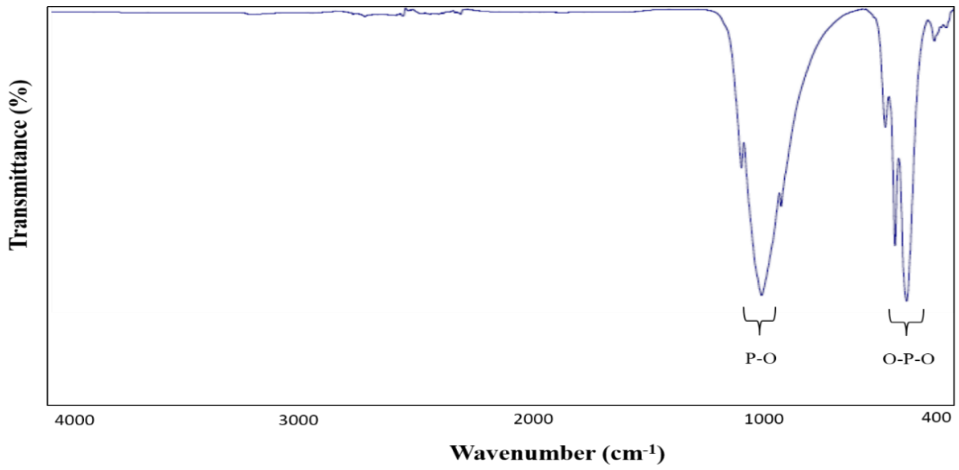


*Figure 3.4.* FT-IR spectra of HA sintered at 1100˚C.

In XRD analysis of CHA, characteristic peaks of CHA were observed (Figure 3.5). For instance, at 2θ=25˚ (0, 0, 2), 2θ=28˚ (1, 0, 2), 2θ=33˚ (3, 0, 0), 2θ=39˚ (2, 1, 2) and 2θ=46˚ (1, 1, 3), CHA was seen (JCPDS No: 00-019-0272) (Wong & Noor, 2016).

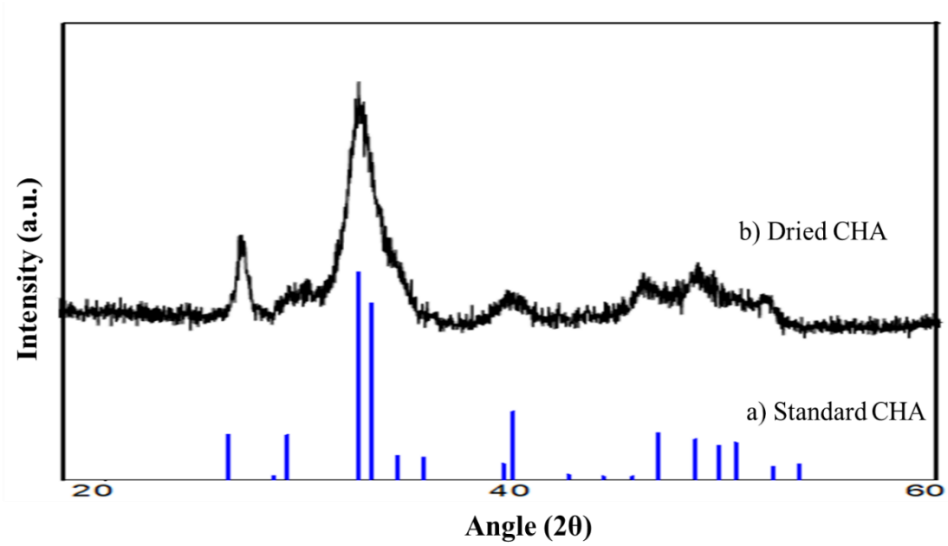


*Figure 3.5.* XRD spectra of CHA: a) Standard of CHA (JCPDS no: 00-019-0272), b) Synthesized CHA after drying.

In FTIR spectrum of CHA, typical vibrations of $CO_3^{2-}$ and $PO_4^{3-}$ groups were observed (Figure 3.6). Absorption bands corresponding to $CO_3^{2-}$ were seen at 872, 1416 and 1644 $cm^{-1}$, while $PO_4^{3-}$ peaks could be seen at 473, 560, 600 and 1018 $cm^{-1}$ (Wong & Noor, 2016; Ezekiel et al., 2018).

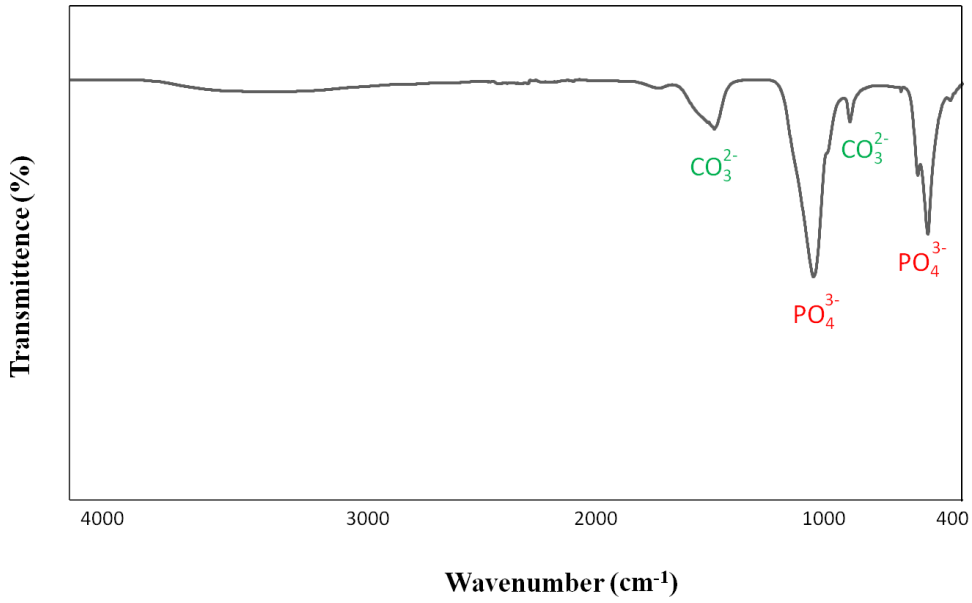


*Figure 3.6.* FT-IR spectra of CHA after drying.

### 3.1.1. Effect of the Milling Time on AKR Particle Size

Particle size analysis was carried out to obtain information about total surface area and particle size of AKR powder. There were differences in terms of surface area, surface weighted mean and volume weighted mean between 1h milling and 10h milling times. (Table 3.1). According to particle size distribution curves there was a group of fine particles (less than 1 µm size) after 10 h milling (Figure 3.7). This was thought to decrease the homogeneity of size distribution. Therefore, all AKR involving groups were milled for 1 h.

Table 3.1. *Effects of different milling times (1h and 10h) on AKR's samples.*

| Samples | Specific surface area ($m^2/g$) | Surface weighted mean D[3,2], µm | Volume weighted mean D[4,3], µm |
|---|---|---|---|
| **AKR-1h** | 0.188 | 31.896 | 47.757 |
| **AKR-10h** | 0.938 | 6.399 | 21.740 |

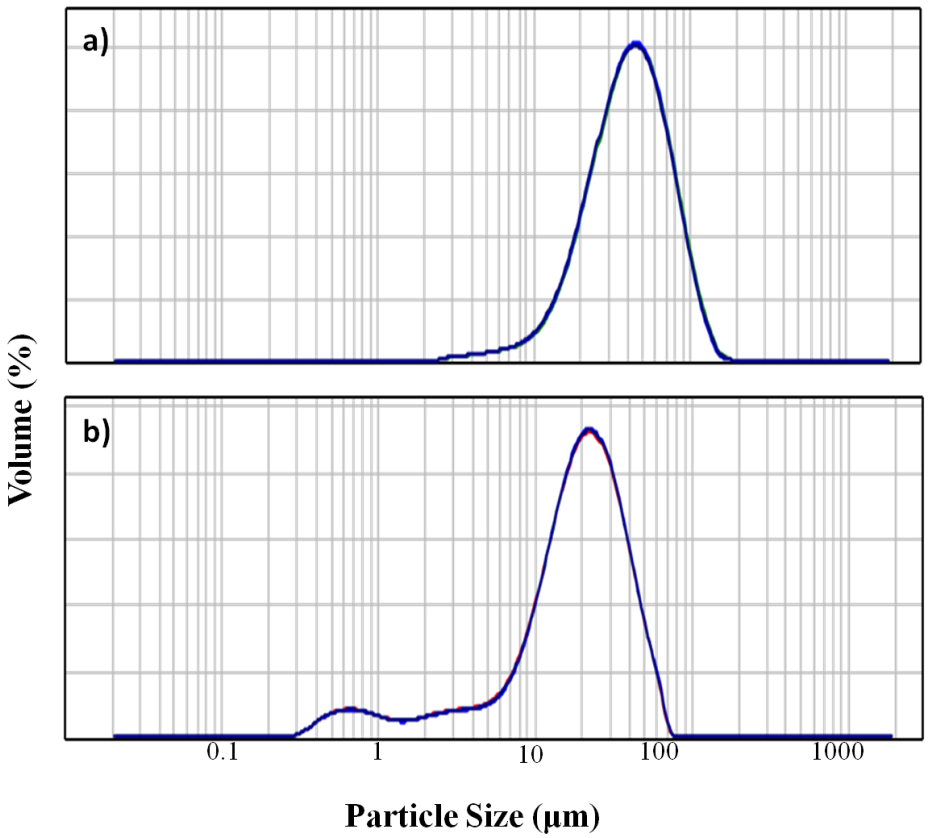


*Figure 3.7.* Particle size distribution of AKR powder. a) after 1h milling, b) after 10h milling.

### 3.2. Analysis of HA:AKR Composites

XRD was applied to all composites of HA:AKR, in order to verify characteristic peaks of both components in composites after milling together (Figure 3.8). XRD analysis results showed that both HA and AKR phases were present in composites. In other words, ball milling did not lead to any change in the structure of HA and AKR

bioceramics. In addition, it was seen that peak intensities of HA:AKR composites were not different from each other. Also, some extra phases were observed. For example, for 90HA10AKR some peaks belonging to tricalcium phosphate were also observed.

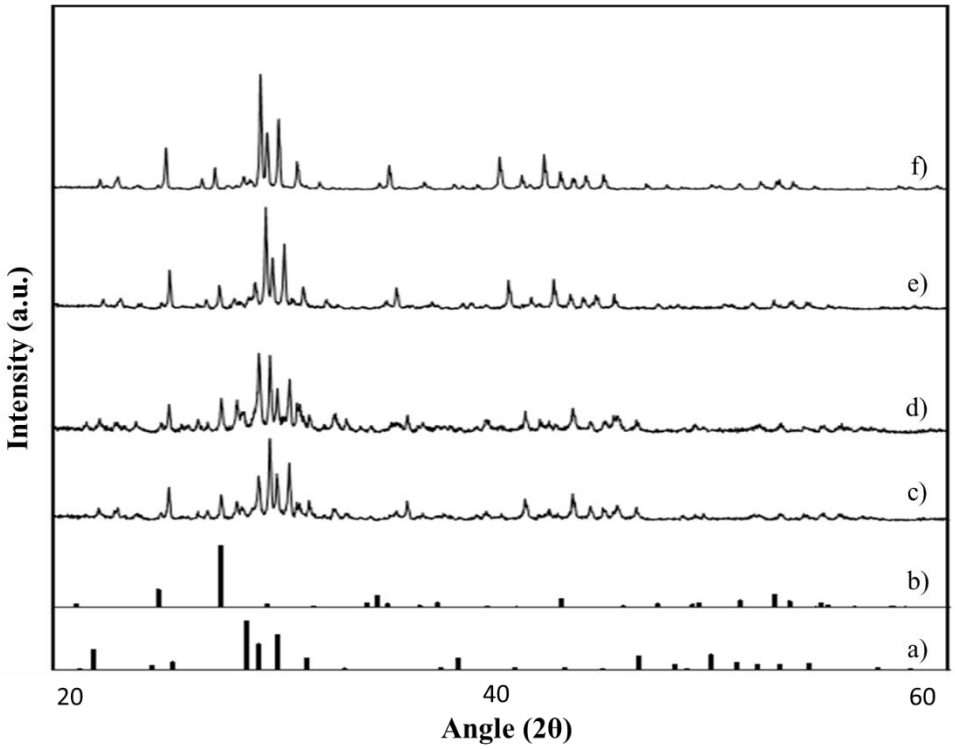


*Figure 3.8.* XRD spectra of all composites after ball milling process: a) Standard HA, b) Standard AKR, c) 33HA66AKR, d) 50HA50AKR, e) 66HA33AKR, f) 90HA10AKR (ICDD number of standard HA: 896439, ICDD number of AKR: 760841).

### 3.3. In Vitro Bioactivity Results of HA, CHA, AKR, HA:AKR and CHA:AKR Samples

In order to investigate apatite layer formation ability of the HA, CHA, AKR, HA:AKR and CHA:AKR samples, they were compressed to disc form and

incubated in SBF for 14 days. Samples from each group were taken at 1, 7 and 14 days and analyzed by SEM. Accordingly, there were apatite formations on the samples (Figure 3.9-3.15). Moreover, Ca/P ratios of the surface formations were examined by EDX for simple minerals and their composites. AKR's Ca/P ratios determined for all immersion times were higher than those of HA and CHA samples at all time points (Table 3.2). In addition, AKR's percent of Ca was higher and percent of P was lower than the others for all immersion times. CHA's Ca/P ratios were closer to original bone apatite. For instance, likewise bone, CHA had a Ca/P ratio of 1.67 at 7$^{th}$ immersion time.

Table 3.2. *Ca/P ratios of minerals formed on HA, CHA and AKR discs after different immersion times in SBF*.

| **Immersion Time (day)** | **HA Ca/P** | **CHA Ca/P** | **AKR Ca/P** |
|---|---|---|---|
| 1 | 1.53 | 1.62 | 2.49 |
| 7 | 1.62 | 1.67 | 3.12 |
| 14 | 1.52 | 1.63 | 2.33 |

The Ca/P ratio of 50HA50AKR composites after 1 day immersion was closer to the ratio for bone apatite Ca/P (1.67) than the other composites and immersion times (Table 3.3). Presence of AKR in composites showed increment trend of Ca/P ratios. For example, it was observed that generally Ca/P ratios were decreasing from 33HA66AKR to 90HA10AKR for all immersion times. Similarly, while simple CHA's Ca/P ratios were around 1.60 (Table 3.2), 90CHA10AKR composite's ratios were 1.71 and 1.83 after 1 and 7 immersion times, respectively (Table 3.3).

Table 3.3. *Ca/P ratios of HA:AKR and CHA:AKR composites at different immersion times in SBF.*

| **Immersion Time (day)** | **33HA66AKR (Ca/P)** | **50HA50AKR (Ca/P)** | **66HA33AKR (Ca/P)** | **90HA10AKR (Ca/P)** | **90CHA10AKR (Ca/P)** |
|---|---|---|---|---|---|
| 1 | 1.86 | 1.60 | 1.64 | 1.58 | 1.71 |
| 7 | 2.14 | 1.99 | 1.86 | 1.54 | 1.83 |
| 14 | 2.68 | 1.85 | 1.73 | 1.55 | 1.60 |

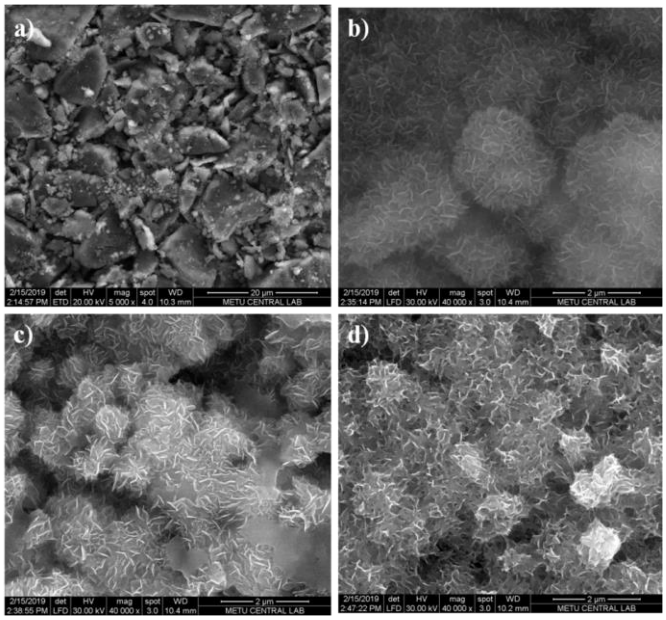


*Figure 3.9.* SEM images of apatite formations on HA discs a) original disc (not immersed in SBF) (Magnification: 5000 X); after different immersion periods in SBF b) 1day; c) 7 days; and d) 14 days (40 000 X).

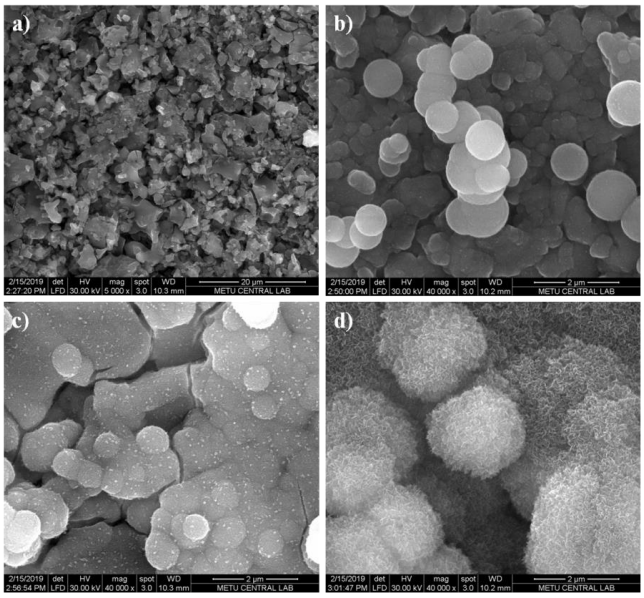


*Figure 3.10.* SEM images of apatite formations on AKR discs a) original disc (not immersed in SBF) (Magnification: 5000 X); after different immersion periods in SBF b) 1day; c) 7 days; and d) 14 days (40 000 X).

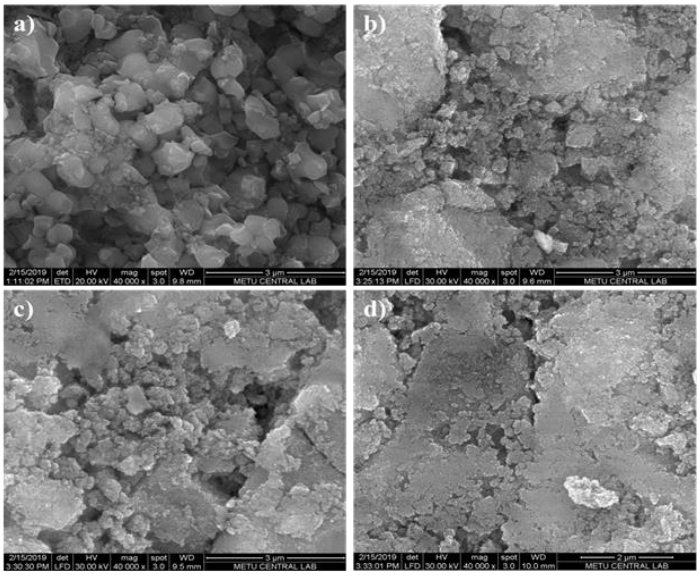


*Figure 3.11.* SEM images of apatite formations on CHA disks for different immersion times in SBF: from a) empty disk (not immerse in SBF) (5000X); b) 1; c) 7 and d) 14 days (40 000X).

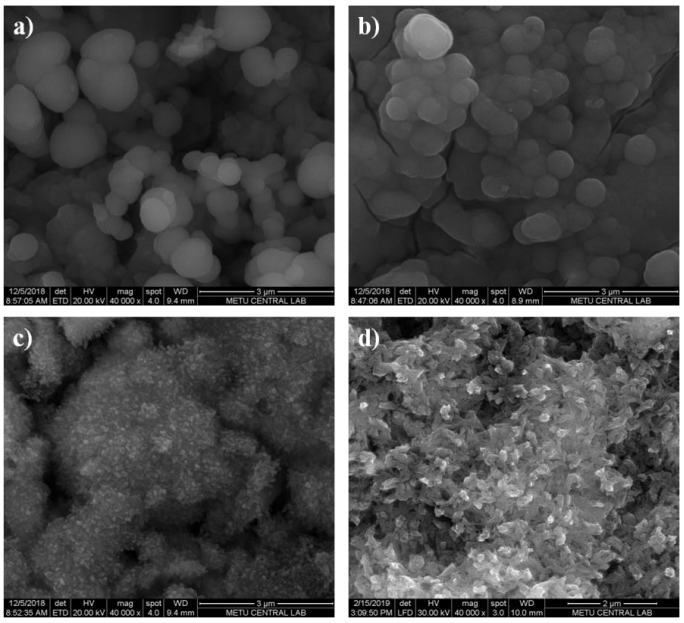


*Figure 3.12.* SEM images of apatite formations on HA:AKR composites for 1 day of immersion time in SBF: from a) 33HA66AKR; b) 50HA50AKR; c) 66HA33AKR and d) 90HA10AKR (40 000X).

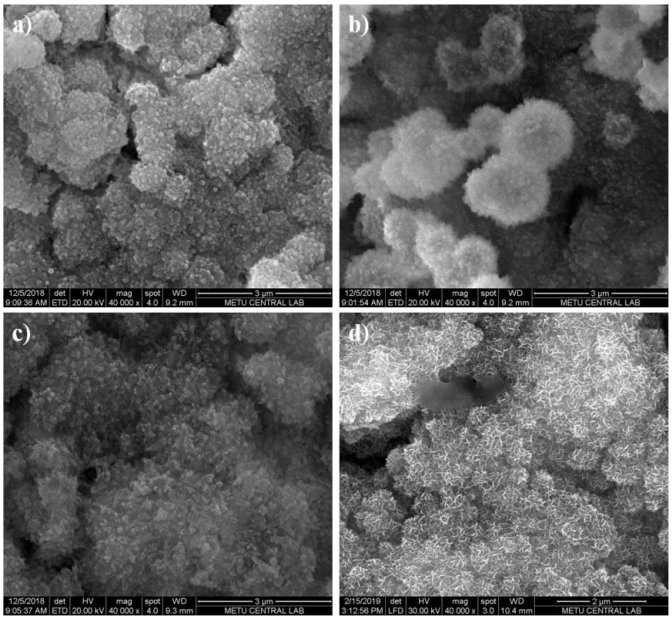


*Figure 3.13.* SEM images of apatite formations on HA:AKR composites for 7 days of immersion in SBF: from a) 33HA66AKR; b) 50HA50AKR; c) 66HA33AKR and d) 90HA10AKR (40 000X).

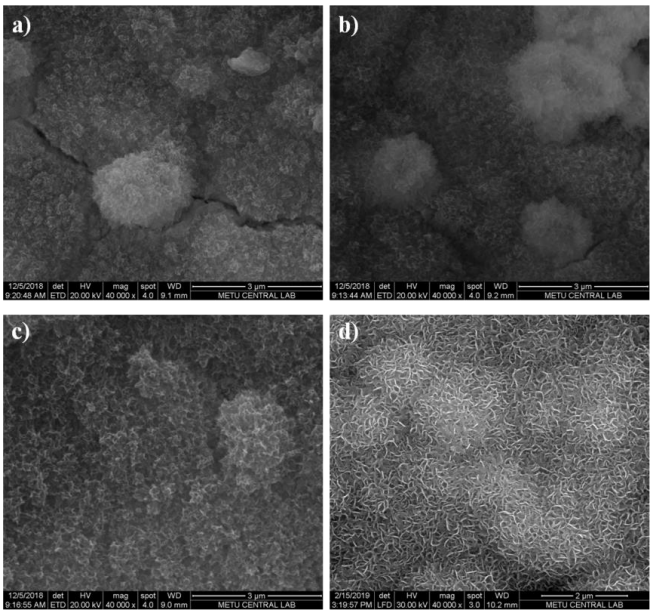


*Figure 3.14.* SEM images of apatite formations on HA:AKR composites for 14 days of immersion in SBF: from a) 33HA66AKR; b) 50HA50AKR; c) 66HA33AKR and d) 90HA10AKR (40 000X).

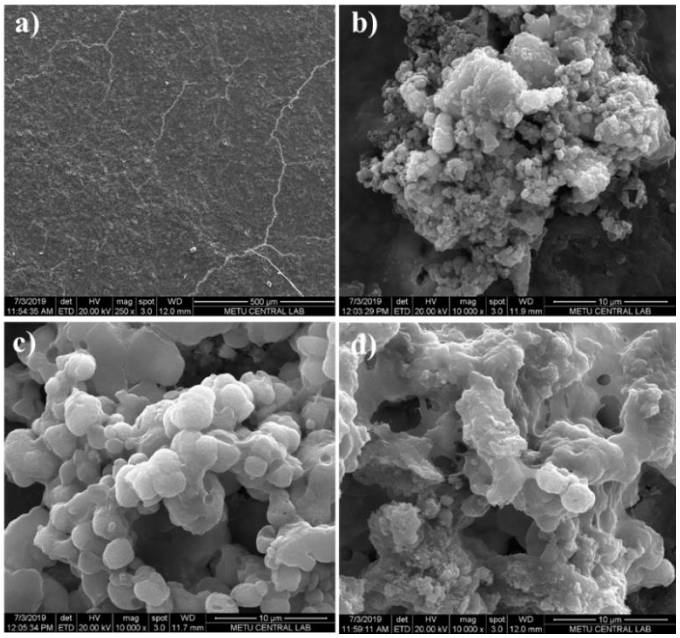


*Figure 3.15.* SEM images of apatite formations on 90CHA10AKR disks for different immersion times in SBF: from a) empty disk (not immerse in SBF) (250X); b) 1; c) 7 and d) 14 days (10 000X).

SEM images (Figure 3.9-15) indicated that all of the simple minerals, HA:AKR composites and CHA:AKR composite were bioactive. Spherical apatite layers were observed on AKR discs. Si elements in the AKR could provide this formation because Si ions have important role as nuclies for apatite formations (Rahmati et al., 2018). For HA:AKR composites the apatite layer formations after 7 days were much more than other incubation periods.

After immersing the samples for different times (1, 7 and 14 days), change in weight of all groups in SBF and PBS was also calculated (Figure 3.16). In all calculations, normalization was done with initial weights. In SBF incubations, while it was not observed that significant changes of HA and AKR of weights for all soaking times, it was seen that CHA's weight increased $7^{th}$ day (Figure 3.16a). This increment can be related to apatite layer formation in surface of disks (Kokubo et al., 1990). Similarly, weight of 90CHA10AKR increased from $1^{st}$ to $14^{th}$, while the other composite groups' weights decreased (Figure 3.16b). In here, this decrease can be related to degradation of HA:AKR composites in SBF. It could be due to rate of apatite formation of 90CHA10AKR being higher than the others. In PBS incubations, the weight of HA did not change from $1^{st}$ to $14^{th}$ soaking time, at $14^{th}$ day weight of AKR increased about 4% according to $1^{st}$ day (Figure 3.16c.). On the other hand, at $14^{th}$ day the weight of CHA decreased about 2%. Similar trend was observed for composite groups. While the weight of HA:AKR ceramics increased a little bit from $1^{st}$ for $14^{th}$ immersion times, the weight of 90CHA10AKR composite decreased (Figure 3.16d). It should be said that there was no any significant degradation for all ceramics and composites of them.

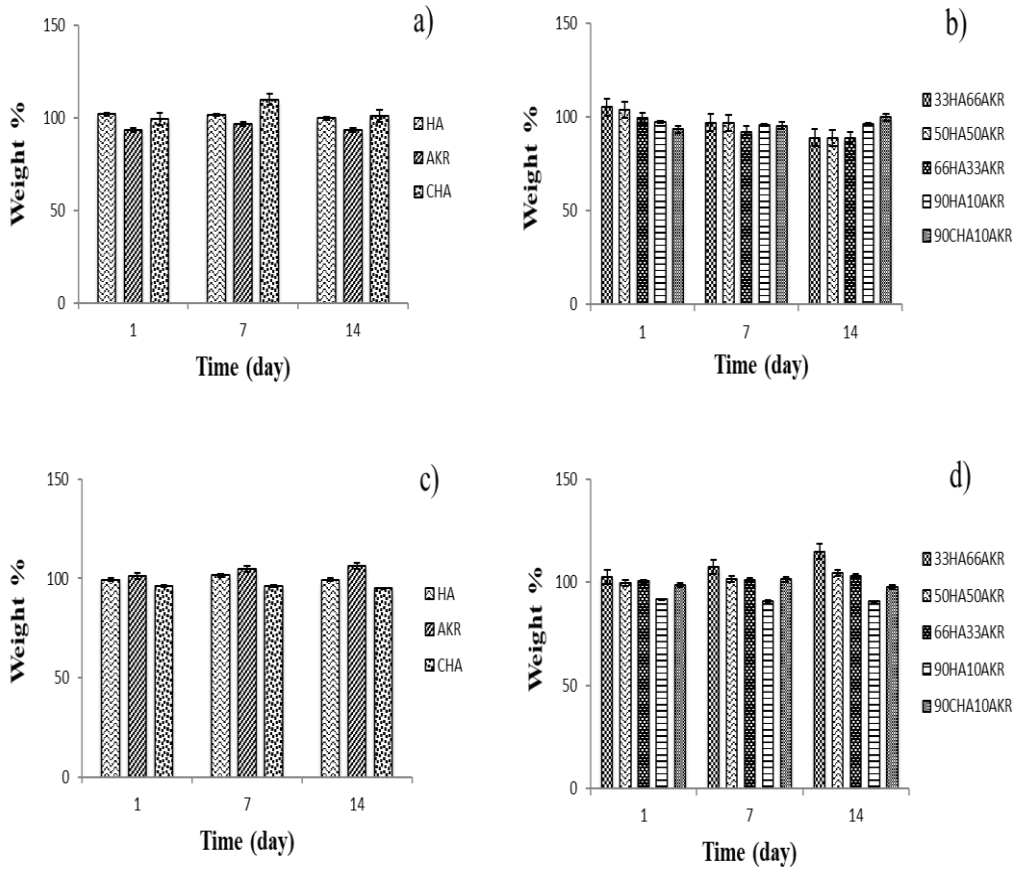


*Figure 3.16.* Weight change of HA, AKR, CHA, HA:AKR and CHA:AKR groups (n=3) a) comparison of weight changes of HA, AKR and CHA samples in SBF, b) comparison of weight changes of HA:AKR and CHA:AKR samples in SBF, c) comparison of weight changes of HA, AKR and CHA samples in PBS and d) comparison of weight changes of HA:AKR and CHA:AKR samples in PBS.

In addition, pH change of incubation media (PBS) was monitored for all groups. According to results, it was shown that AKR led to an increase in pH. While pH value was about 7.40 for HA and CHA at all times, AKR formed pH values of about 10-11 (Figure 3.17a). For instance, the pH of the PBS increased from 7.4 to 11 after 1 day of soaking. Furthermore, as the amount of AKR was increased in compositions, the pH level increased accordingly (Figure 3.17b). This increment can be related with $OH^-$ concentration; $OH^-$ concentration could increase because of exchange of $Ca^{2+}$

with $H^+$ ions (Rahmati et al., 2018). Apatite formation is also related to $OH^-$ ions concentration in the surrounding solution. In other words, an increase in the pH of the solution could induce the deposition of apatite on the ceramic surface (Rahmati et al., 2018; Kokubo et al., 1990).

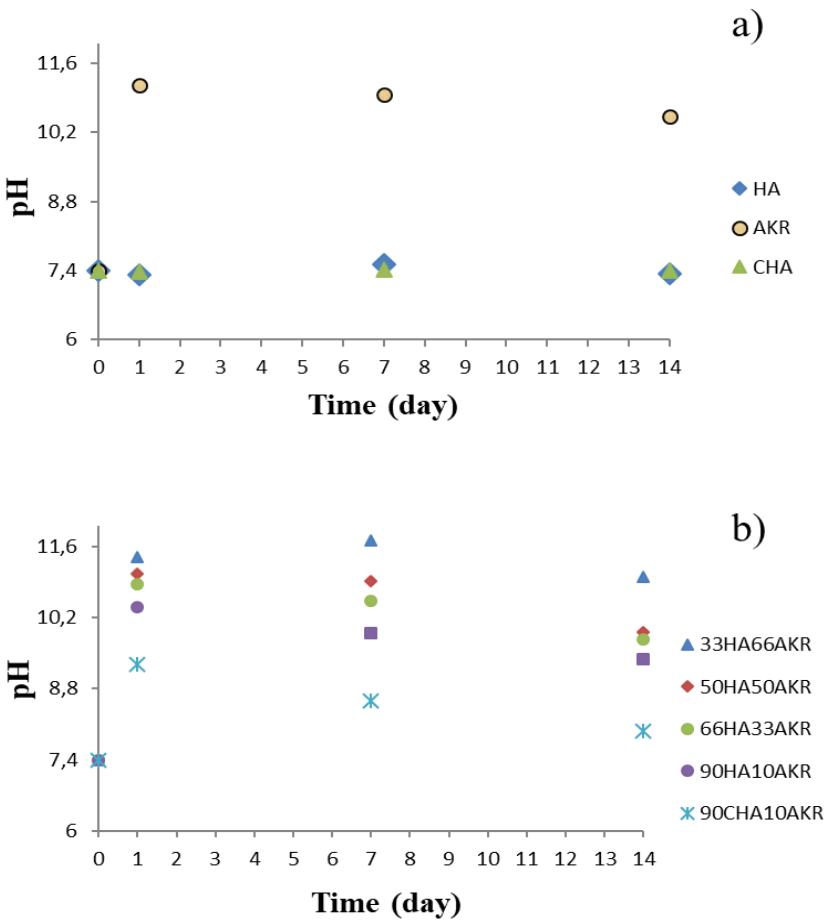


Figure 3.17. pH change of samples in PBS for 1, 7 and 14 days. a) Only HA, AKR and CHA ceramics, b) HA:AKR and CHA:AKR composites.

In order to obtain an approximate information about swelling of bioceramics, swelling ratio (SR) was calculated from the wet weight of disks of HA, AKR, CHA and all

composites at different time points. Although no significant differences were observed, results showed that SR of CHA involving groups was higher than that of only HA and AKR (Table 3.4.). Similarly, swelling ratio of 90CHA10AKR composite was higher than that of HA:AKR composites. In addition, AKR ceramics swelled more than HA. Likewise, as seen in Table 3.4, swelling level increases as AKR increase in composites.

Table 3.4. *Swelling ratios of HA, AKR, CHA and all composites (n=3).*

| **Samples** | **1st Day (%)** | **7th Day (%)** | **14th Day (%)** |
|---|---|---|---|
| HA | 14±3 | 14±3 | 14±3 |
| AKR | 21±2 | 21±2 | 20±2 |
| CHA | 38±2 | 37±3 | 32±3 |
| 33HA66AKR | 23±3 | 22±3 | 22±3 |
| 50HA50AKR | 22±3 | 21±3 | 21±3 |
| 66HA33AKR | 20±2 | 20±2 | 19±2 |
| 90HA10AKR | 16±3 | 16±3 | 16±3 |
| 90CHA10AKR | 29±2 | 32±2 | 34±3 |

### 3.4. Results of Diametral Compression Testing

Diametral strength test is alternative mechanical test to bending test for ceramics due to simplicity in practice and availability in test sample preparation (Bigi et al., 1992; Amoros et al., 2008). This type of mechanical test is proper for biomedical interests such as dental and orthopedic applications due to similarity between stresses formed *in vivo* for dental implants and stresses generated by diametral compression test (Speirs et al., 2005; Xu et al., 2007).

Table 3.5. *Results of diametral tensile strength of bioceramics groups.*

| Bioceramics and Their Composites Groups | Diametral Tensile Strength (MPa) |
|---|---|
| HA | 2.48±0.15 |
| AKR | 0.74±0.04 |
| CHA | 1.44±0.02 |
| 90HA10AKR | 0.80±0.05 |
| 90CHA10AKR | 1.42±0.11 |

In table 3.5, average diametral tensile strengths (MPa) of ceramics groups are illustrated. Results showed that diametral strength of HA was higher than the others. AKR had the lowest diametral strength. Many factors such as porosity, sintering temperature, grain size, presence of second phase and presence of impurities could affect the diametral strength. For example, generally if sintering temperature increases, then the diametral strength also increase (Basar, 2009). When observed Table 3.5, it is seen that 90CHA10AKR composite is stronger than 90HA10AKR. Presence of AKR in 90HA10AKR composite led to decreasing strength while presence of

AKR in 90CHA10AKR composite did not negatively affect strength. Difference of porosity between HA and CHA, grain size or second phases in HA (i.e. tricalciumphosphate) and AKR (i.e. diopside or merwinite) could bring about this result (Basar, 2009; Evis & Ozturk, 2008; Bigi et al., 1992).

### 3.5. Results of Optimization Studies for Electrospun PCL Scaffolds

To analyze micro structure and fiber characteristics of PCL scaffolds obtained by electrospinning, SEM analysis was applied to all tested concentrations of PCL; 10%, 15% and 20% (Figure 3.18). Microscopic observations revealed while the first 2 concentration groups had fiber fusion in their structure (Figure 3.18a, b, c), 20% PCL group did not have any fusion (Figure 3.18d). According to this figure there was a tendency towards decreasing bead like thickenings in fiber structures and also in fiber fusion with the increase in concentration of PCL. The last group also had very

distinctive nano- and micro-sized fibers in its structure which is known to be necessary for supporting cell attachment as well as providing suitable diffusion environment (Venugopal et al., 2019). In addition, although having very smooth and uniform fibers in terms of thickness is accepted advantageous, heterogeneous structure of fibers such as micro and nano sizes or the presence of some beads can provide unique features such as higher mechanical properties and surface roughness (Esmailian et al., 2018).

Therefore, 20 % PCL group was found as most the suitable group in terms of structural and morphological properties for preparation of bioceramics loaded scaffolds. As seen in Figure 3.18d, both nano- and micro- sized fibers such as 262.3 nm, 577 nm and 1.36 μm were observed.

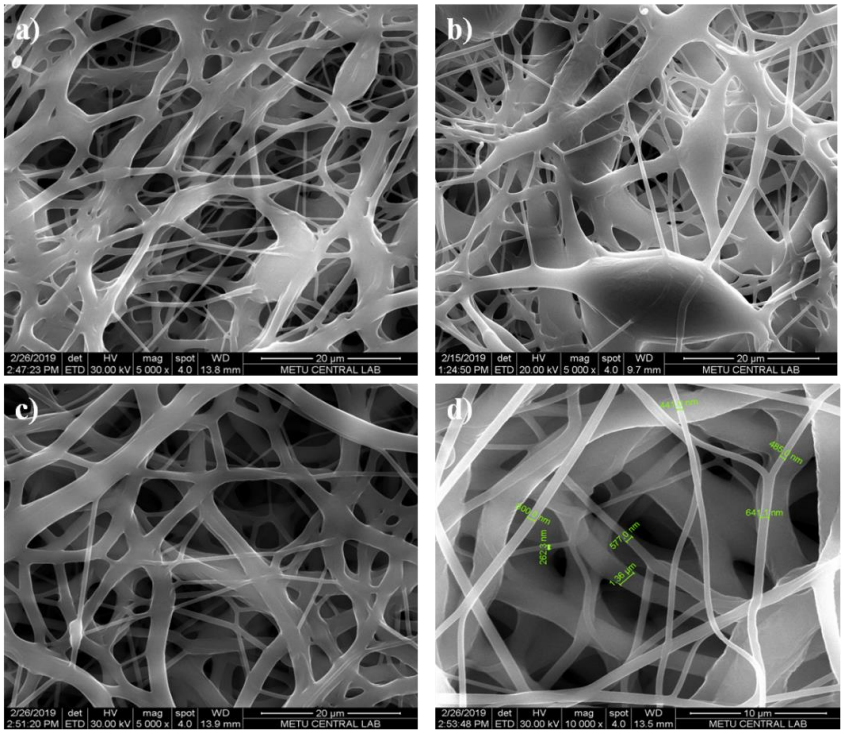


Figure 3.18. SEM images of PCL scaffolds: a) 10% PCL, b) 15% PCL, c) 20% PCL (Magnification: 5 000 x) and d) 20% PCL/acetone with sizes of fibers (Magnification: 10 000 x).

Furthermore, after optimization of PCL concentration, different amounts of ceramics added into PCL solution before electrospinning. For example, 8% of 90HA10AKR and 10% 90HA10AKR bioceramics were spun with 20% of PCL. To observe differences between them, SEM analysis was applied. SEM images showed that 10% 90HA10AKR loaded PCL fibers had homogeneous distribution than 8% 90HA10AKR (Figure 3.19).

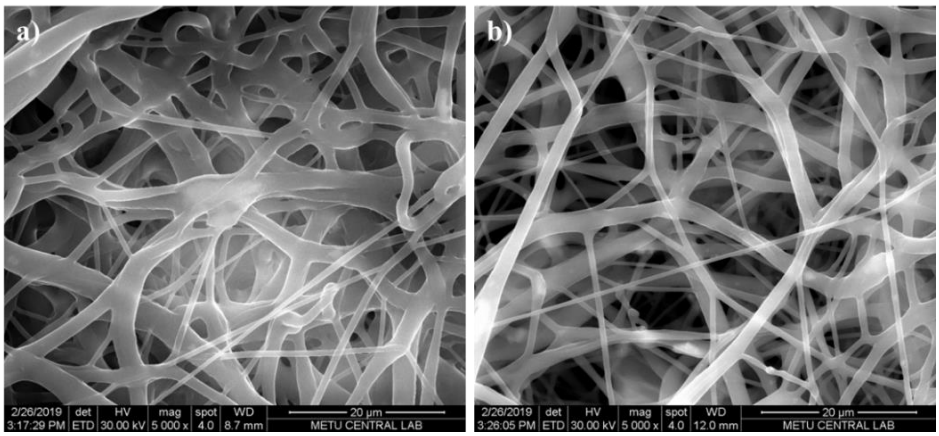


Figure 3.19. SEM images of different percent of 90HA10AKR ceramics loaded in 20% PCL fibers: a) 8% 90HA10AKR, b) 10% 90HA10AKR (Magnification: 5 000 x).

### 3.6. Bioactivity and Degradation Results of Bioceramic Loaded PCL Scaffolds

The growing bone-like apatite layer at the tissue implant interface is a prerequisite for the adhesion of biomaterials to the bone and can induce a good environment for living bone formation (Wu et al., 2019). There is a correlated relation between rate of apatite formation and the degree of bone bioactivity of biomaterial in vivo (Kokubo & Takadama, 2006). Therefore, in order to observe apatite layer formation ability of the scaffolds, scaffolds were immersed in SBF for 1, 7 and 14 days at 37˚C. In all groups: 20% of PCL (in acetone) and 10% of minerals (in PCL/acetone solution). SEM analysis showed that there was no bone-like apatite layer formation at 1$^{st}$ day for all scaffold groups. While there were apatite formations on the PCL/CHA and

PCL/90CHA10AKR fibers for 7$^{th}$ and 14$^{th}$ days (Figure 3.20-24), there were no apatite formation present on PCL scaffold without minerals and PCL/HA scaffold. For PCL/90HA10AKR scaffold, bone-like apatite layer formations were seen at 14$^{th}$ day. In addition, some deformations were observed in PCL scaffold without minerals and PCL/HA scaffold for 7$^{th}$ and 14$^{th}$ days (Figure 3.20 and 3.21). However, there were not any deformations in PCL/90HA10AKR and PCL/90CHA10AKR for all incubation periods. Presence of AKR and CHA could have provided apatite layer formation and prevent deformations of fibers. Scaffolds loaded with CHA and AKR minerals also showed higher mineralization at 7$^{th}$ and 14$^{th}$ days.

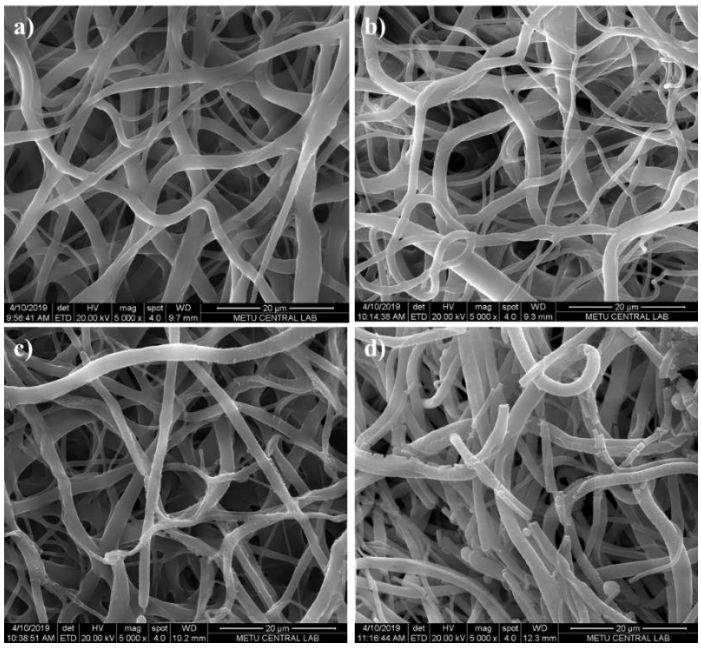


Figure 3.20. SEM images of PCL scaffolds a) (not immersed in SBF), b) 1 day, c) 7 days and d) 14 days after incubation in SBF (Magnification: 5000 x).

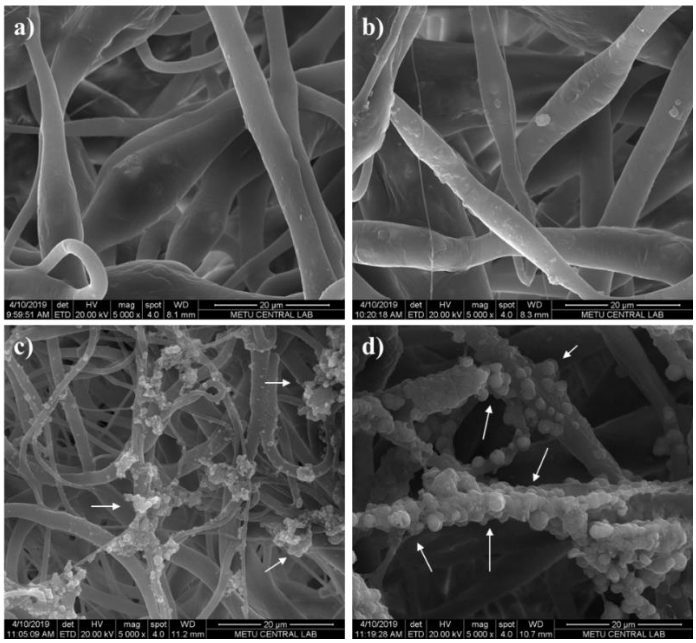


Figure 3.21. SEM images of PCL/CHA scaffolds a) (not immersed in SBF), b) 1 day, c) 7 days and d) 14 days after incubation in SBF (Magnification: 5000 x). (Arrows: Apatite formations).

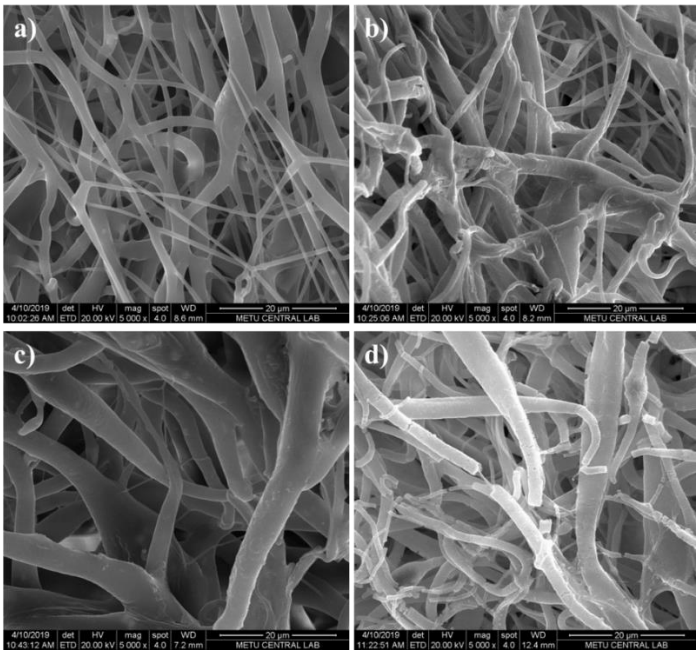


Figure 3.22. SEM images of PCL/HA scaffolds a) (not immersed in SBF), b) 1 day, c) 7 days and d) 14 days after incubation in SBF (Magnification: 5000 x).

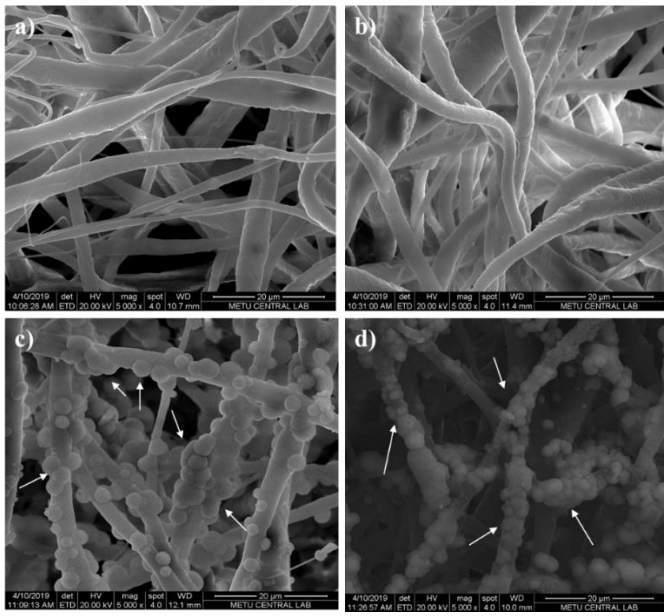


Figure 3.23. SEM images of PCL/90CHA10AKR scaffolds a) (not immersed in SBF), b) 1 day, c) 7 days and d) 14 days after incubation in SBF (Magnification: 5000 x). (Arrows: Apatite formations).

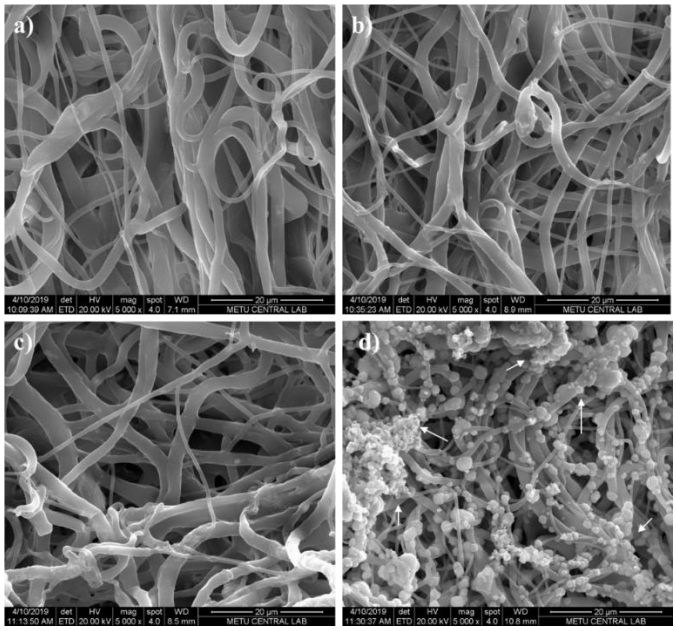


*Figure 3.24.* SEM images of PCL/90HA10AKR scaffolds a) (not immersed in SBF), b) 1 day, c) 7 days and d) 14 days after incubation in SBF (Magnification: 5000 x). (Arrows: Apatite formations).

Furthermore, weight change of scaffolds of each group was also quantified for 1, 7 and 14 days of SBF incubations. Generally, in all groups, it was found that average weights increased from 1 to 7 soaking times in all groups except PCL group. However, especially, in PCL/CHA (17% increased at $14^{th}$ day according to $1^{st}$ day) and PCL/90CHA10AKR (27% increased at $14^{th}$ day according to $1^{st}$ day) average weight increased considerably (Figure 3.25a). This increment trend can be related with mineralization on fiber surfaces. Meanwhile, for testing of degradation of fibers, experiments including incubation in PBS were also done. Average weight of scaffolds for each group was obtained and compared for 1, 7 and 14 days. Results of degradation analysis represented that there was no significant change on weight (Figure 3.25b). Lack of enzymes in the PBS solution could lead to this matter (Bosworth & Downes, 2010). For example, PCL solvent cast films immersed in PBS including lipase Gan et al., 1997). At the end of the study, they observed that PCL films degraded completely after 4 days (Gan et al., 1997). In addition, the structure of PCL has significance in terms of degradation rate (Bölgen et al., 2005). In other words, Bölgen et al. found that morphology of PCL affects the degradation rate. Their study showed that electrospun fibres demonstrated slow degradation. PCL fibres are very hydrophobic. Therefore, this case brought about reducing surface hydrolysis and the diffusion of water molecules into the fibres (Bölgen et al., 2005).

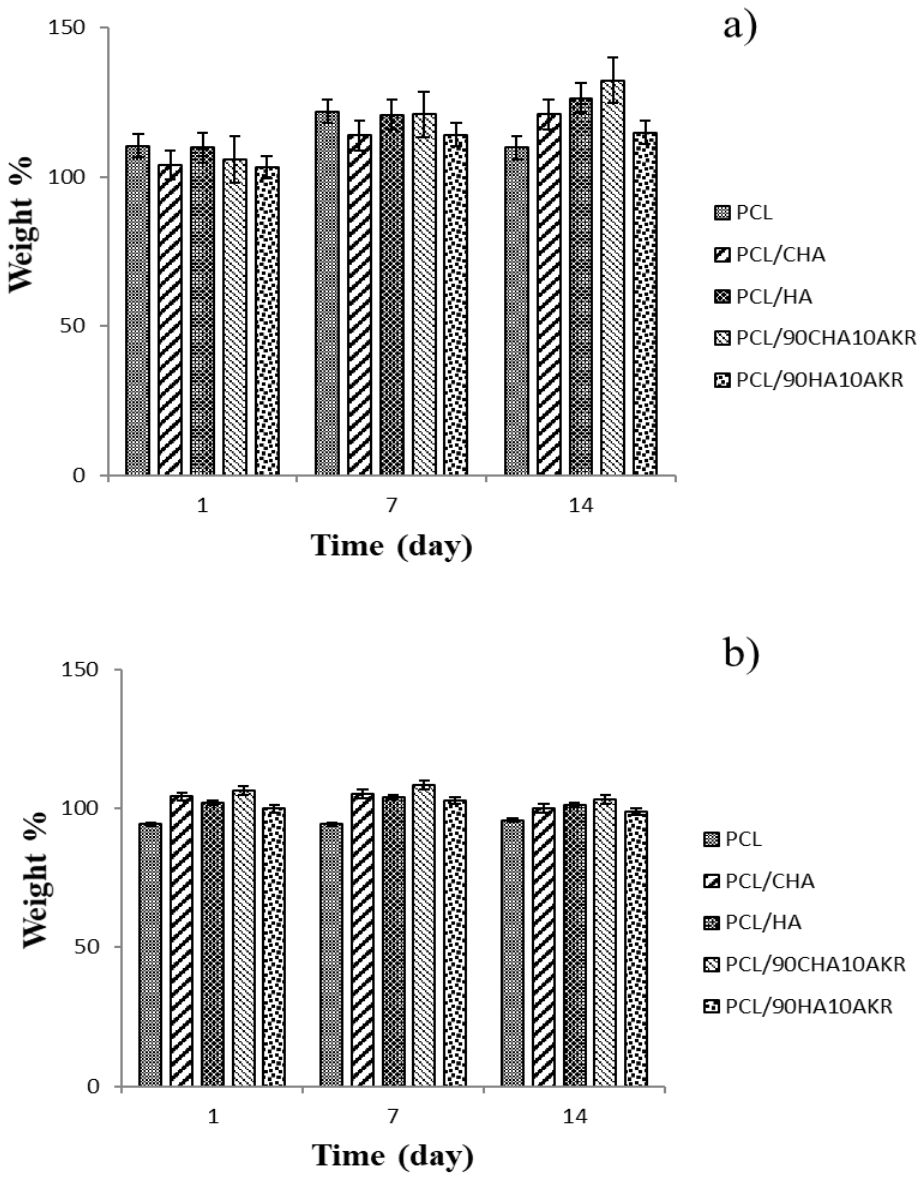


Figure 3.25. Average weight change of fiber groups (n=3) in SBF and PBS. a) weight changes of samples in SBF, and b) weight changes of samples in PBS.

During degradation analysis, pH change of incubation environment was also measured. It was revealed that, there were no significant change in pH values for all groups (Table 3.6).

Table 3.6. *Average pH values of scaffold groups during degradation analysis.*

| Scaffold Groups | 0 day | 1st day | 7th day | 14th day |
|---|---|---|---|---|
| PCL | 7.40±0.02 | 7.41±0.02 | 7.33±0.04 | 7.33±0.03 |
| PCL/CHA | 7.40±0.03 | 7.40±0.02 | 7.35±0.04 | 7.30±0.02 |
| PCL/HA | 7.40±0.02 | 7.41±0.04 | 7.36±0.03 | 7.33±0.02 |
| PCL/90CHA10AKR | 7.40±0.04 | 7.43±0.03 | 7.34±0.04 | 7.33±0.04 |
| PCL/90HA10AKR | 7.40±0.04 | 7.49±0.04 | 7.33±0.01 | 7.34±0.05 |

Furthermore, to obtain an approximate information about swelling of scaffold groups, SR was calculated from the wet weight of fibers of PCL, PCL/CHA, PCL/HA, PCL/90CHA10AKR and PCL/90HA10AKR polymer-bioceramics composites at different time points. Results showed that if there were bioceramics into PCL, then SR would decrease. As seen in Table 3.7 only PCL had much more SR than all of scaffolds (Table 3.7). PCL/CHA scaffolds had more SR than PCL/HA. Similarly, it was observed that SR of PCL/90CHA10AKR composite was higher than that of PCL/90HA10AKR composites.

Table 3.7. *SR of PCL/Bioceramic composites (n=3).*

| Samples | Day 1 (%) | Day 7 (%) | Day 14 (%) |
|---|---|---|---|
| PCL | 243±10 | 283±10 | 207±10 |
| PCL/CHA | 61±5 | 105±5 | 125±5 |
| PCL/HA | 38±5 | 43±5 | 74±5 |
| PCL/90CHA10AKR | 87±5 | 129±5 | 108±5 |
| PCL/90HA10AKR | 37±5 | 47±5 | 50±5 |

## 3.7. Cell Culture Studies

### 3.7.1. Cell Viability

Proliferation of Saos-2 cells on the scaffolds was determined using Alamar Blue cell viability assay for 1, 4 and 7 days (Figure 3.26). All scaffolds' cell viability results showed and increment trend. It can be said that scaffolds groups do not have any

cytotoxicity effect on Saos-2 cells (Dalgic et al., 2018). However, especially PCL/90CHA10AKR and PCL/90HA10AKR fibers represented significantly higher cell viability in 7 days compared to other groups. Studies showed that the Si ions from bioactive glass or bioactive ceramics increased cell proliferation (Sun et al., 2006). Also, Mg containing bioceramics use in orthopedic implantations due to inducing of adhesion of osteoblastic cells (Zreiqat et al., 2002). AKR includes Si, Mg and Ca, so these ions could promote cell proliferation (Sun et al., 2006). SEM analysis showed cell's adherence and spread for 1 and 7 days (Figure 3.27-3.31).

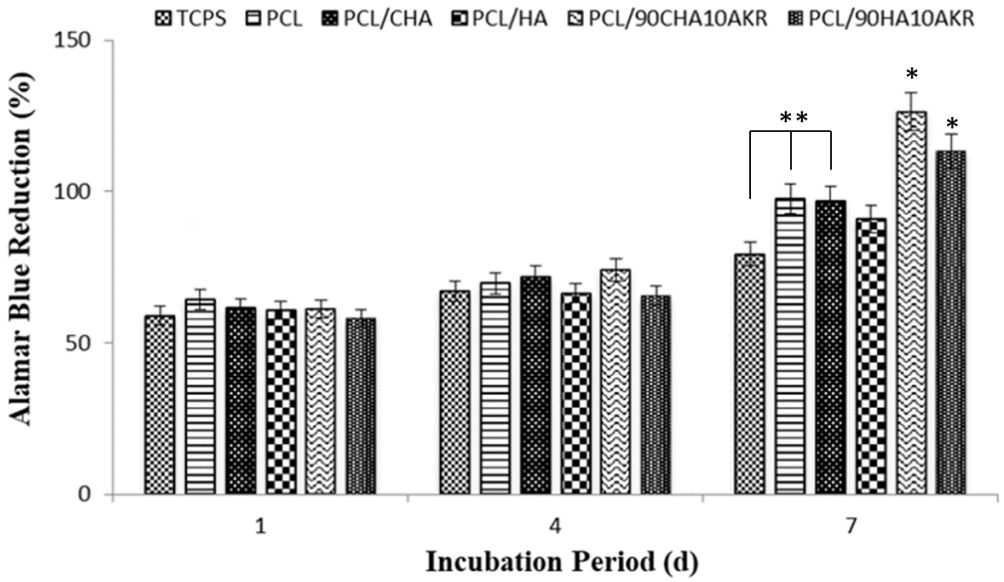


Figure 3.26. Alamar Blue reduction results of scaffold groups after 1, 4 and 7 days of incubation with Saos-2 cells. * Significant difference of the PCL/90CHA10AKR and PCL/90HA10AKR group from all groups after 7 days of profileration ($p<0.01$). ** Significant difference of the TCPS from PCL and PCL/CHA ($p<0.05$) (n=4).

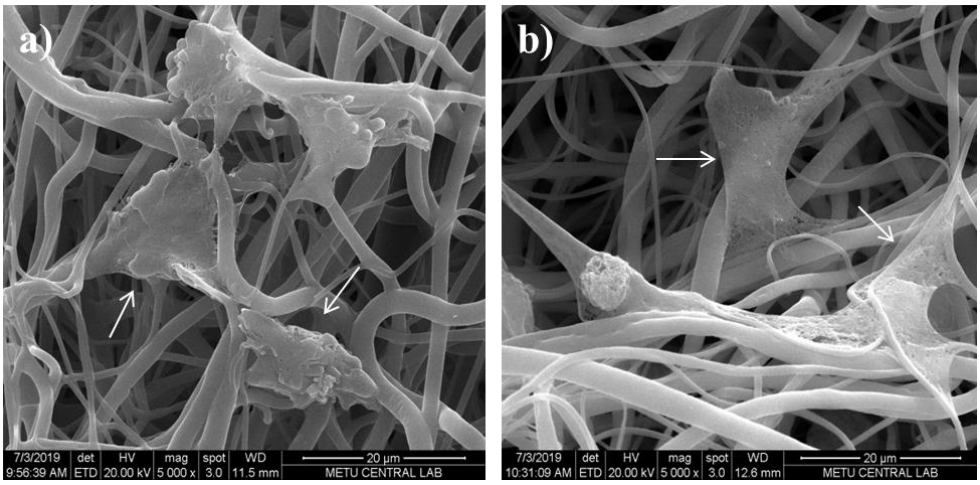


Figure 3.27. SEM images of Saos-2 cells on the PCL scaffolds; 1 days a) (Magnification: 5 000 x), 7 days b) (Magnification: 5 000 x). (Arrows: Adhered and spread cells).

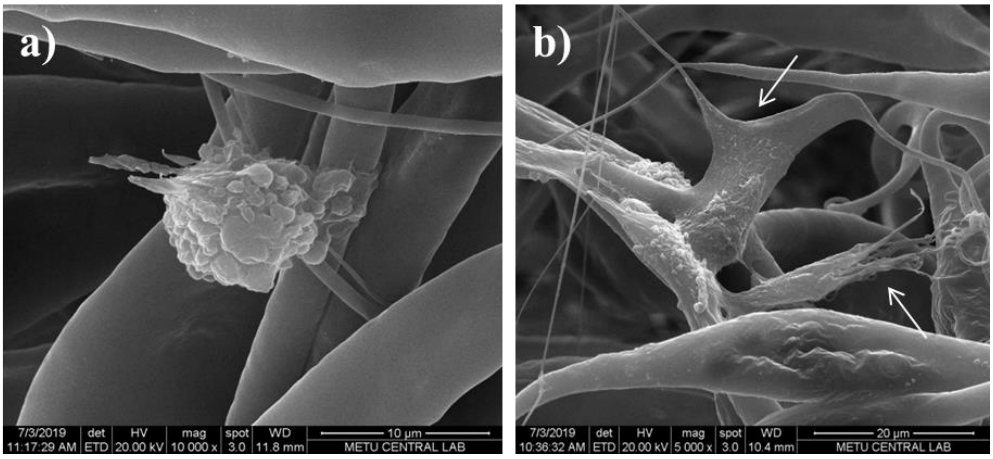


Figure 3.28. SEM images of Saos-2 cells on the PCL/CHA; 1 days a) (Magnification: 10 000 x), 7 days b) (Magnification: 5000 x). (Arrows: Adhered and spread cells).

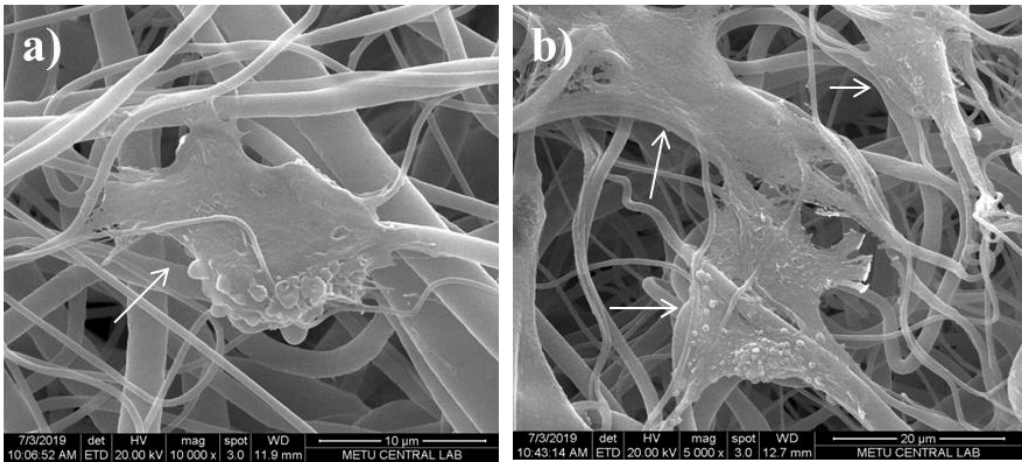


*Figure 3.29.* SEM images of Saos-2 cells on the PCL/HA; 1 days a) (Magnification: 10 000 x), 7 days b) (Magnification: 5 000 x). (Arrows: Adhered and spread cells).

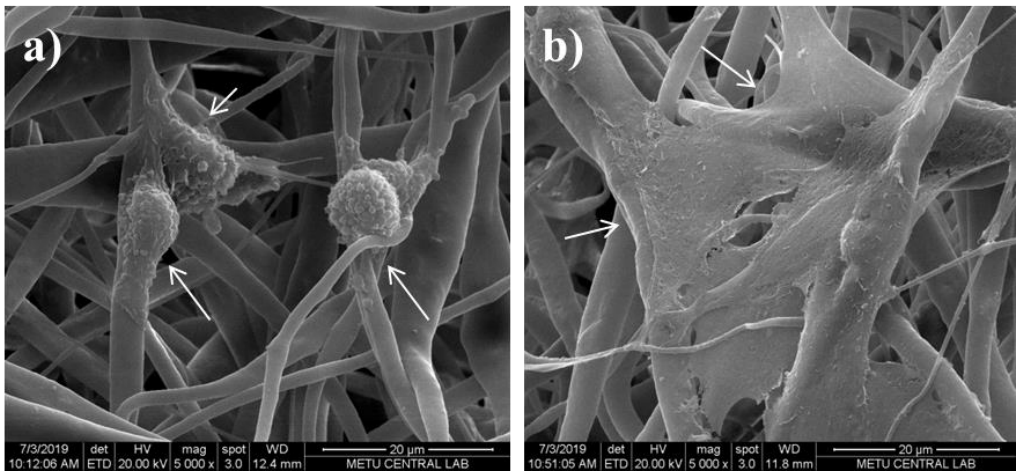


Figure 3.30. SEM images of Saos-2 cells on the PCL/90CHA10AKR; 1 days a) (Magnification: 5 000 x), 7 days b) (Magnification: 5 000 x). (Arrows: Adhered and spread cells).

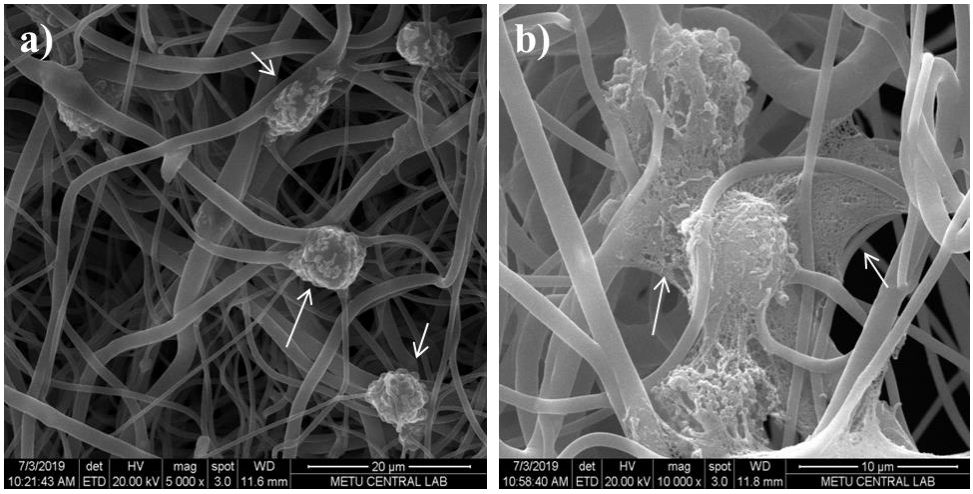


*Figure 3.31.* SEM images of Saos-2 cells on the PCL/90HA10AKR; 1 days a) (Magnification: 5 000 x), 7 days b) (Magnification: 10 000 x). (Arrows: Adhered and spread cells).

### 3.7.2. Osteogenic Activity of Cells

All Saos-2 cell seeded on scaffold groups showed ALP activity until 2$^{nd}$ week (Figure 3.32). In other words, ALP activity of cells increased at 14$^{th}$ day. However, cells seeded on PCL/CHA fibers showed higher ALP activity than the others at 2$^{nd}$ week. Calcium and phosphate rich environment from CHA could provide to increase ALP activity of the Saos-2 cells (Mohammad et al., 2016). In Figure 3.32, it is seen that cell seeded TCPS showed higher ALP activity than the scaffolds groups for 7 and 14 days. This situation can be related with dimension of surfaces. While TCPS have 2 dimensional structure, scaffolds have 3-dimensional shape. Hence, cells could show easier osteogenic activity on TCPS than the scaffolds. Furthermore, when observed ALP activity graph (Figure 3.32), it is seen that activity of cells at 7$^{th}$ day is lower than 14$^{th}$ day. This situation can be related with cell viability studies. In Alamar reduction graph (Figure 3.26), it is observed that cell viability highly increased especially for PCL/90CHA10AKR and PCL/90HA10AKR scaffold groups at 7$^{th}$ day. his means that observation of lower ALP activity at 7$^{th}$ day is predictable.

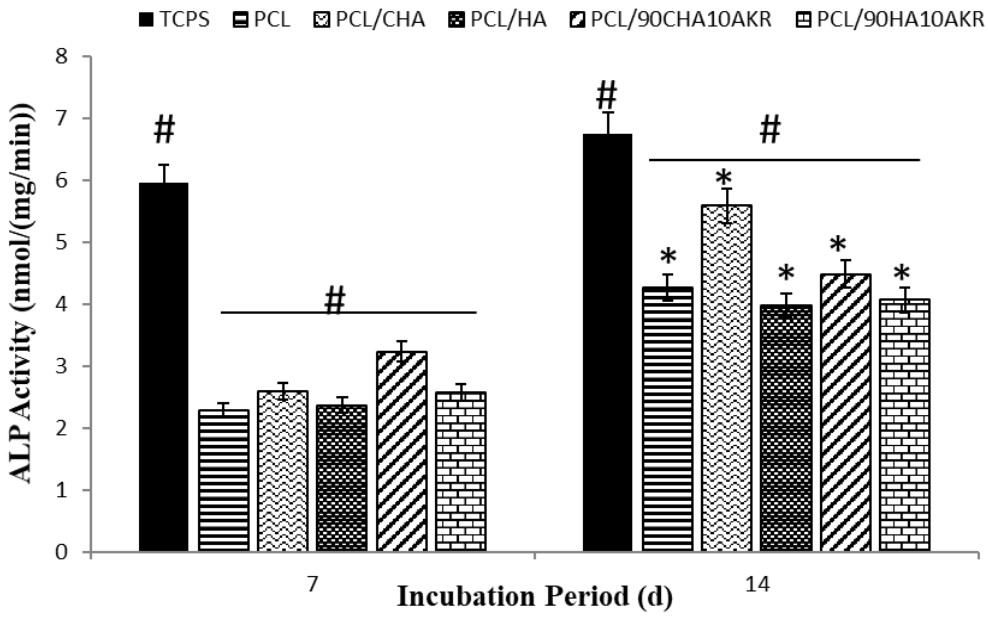


*Figure 3.32.* Specific ALP activity of seeded Saos-2 cells on the scaffolds after 7 and 14 days of incubation. # TCPS is different from all other scaffold groups ($p<0.01$). * PCL/CHA different from all other scaffold groups ($p<0.01$). (n=4).

In addition, SEM analysis for 7$^{th}$ and 14$^{th}$ days revealed that there are cellular differentiations and mineralization on the Saos-2 cells seeded scaffolds (Figure 3.33-37). SEM results showed cells were spread on the all scaffolds groups at 7$^{th}$ and 14$^{th}$ days. It was shown that there was much more mineralization on the PCL/90CHA10AKR and PCL/90HA10AKR scaffolds than the other groups at 14$^{th}$ day in osteogenic medium. Cells had almost covered the surface even at 7$^{th}$ day. Moreover, fibers were almost not visible at 14$^{th}$ day due to cell growth and spread. In here, dissolution of ionic products of AKR such as Si, Mg and Ca could promote cell adhesion, proliferation and growth (Bakhsheshi-Rad et al., 2019b).

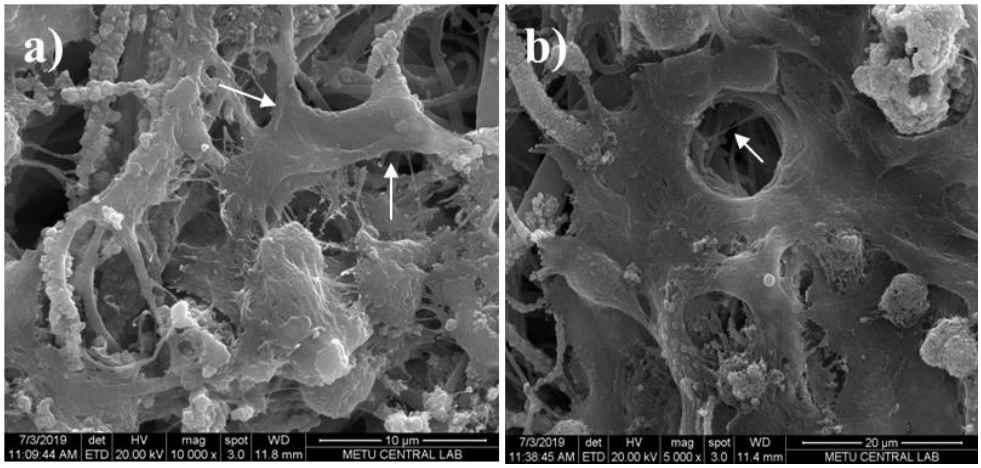


Figure 3.33. SEM images of Saos-2 cells on PCL scaffolds after incubation periods; 7 days a) (10 000 x), 14 days b) (5 000 x). (Arrows: Spread cells).

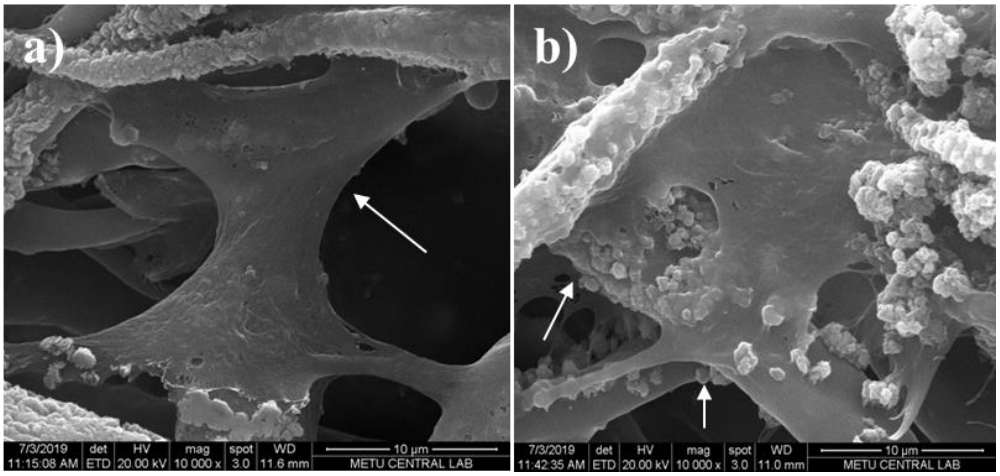


Figure 3.34. SEM images of Saos-2 cells on PCL/CHA scaffolds after incubation periods; 7 days a) (10 000 X), 14 days b) (10 000 X). (Arrows: Spread cells).

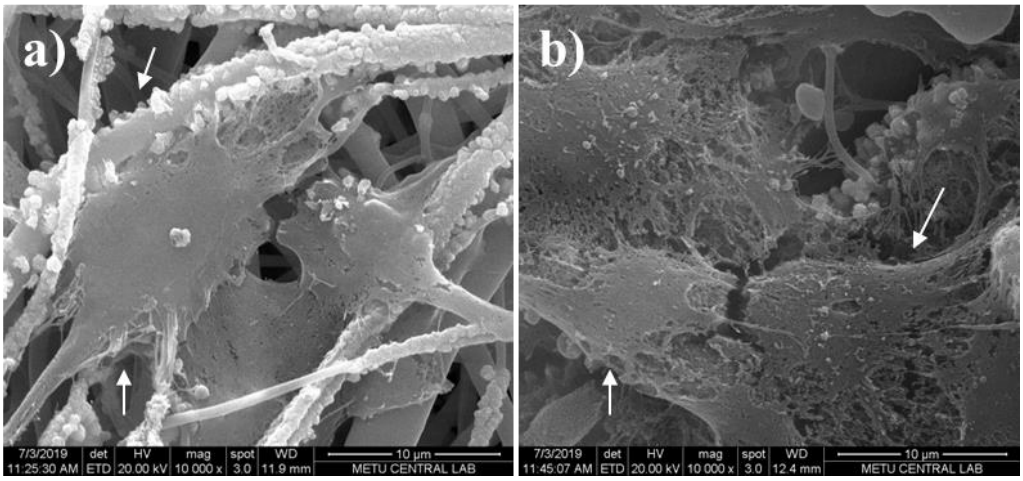


*Figure 3.35.* SEM images of Saos-2 cells on PCL/HA scaffolds after incubation periods; 7 days a) (10 000 x), 14 days b) (10 000 x). (Arrows: Spread cells).

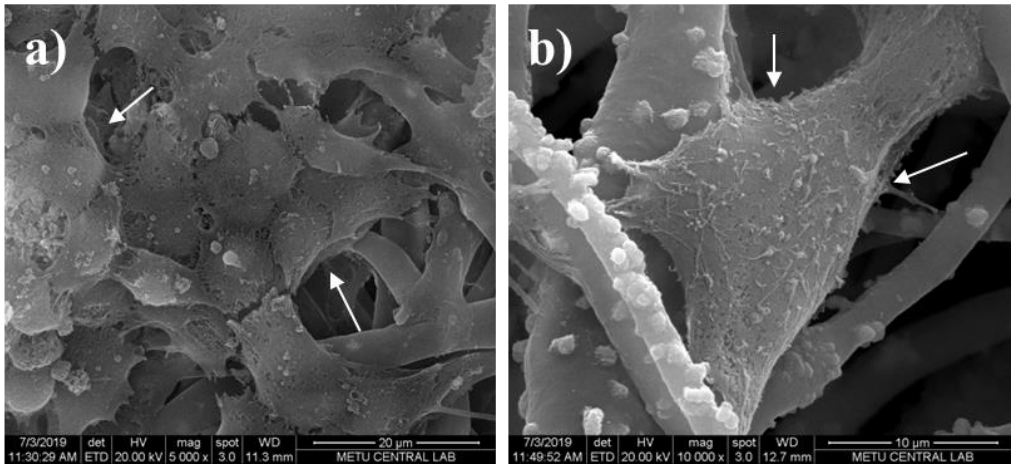


*Figure 3.36.* SEM images of Saos-2 cells on PCL/90CHA10AKRscaffolds after incubation periods; 7 days a) (5 000 X), 14 days b) (10 000 x). (Arrows: Spread cells).

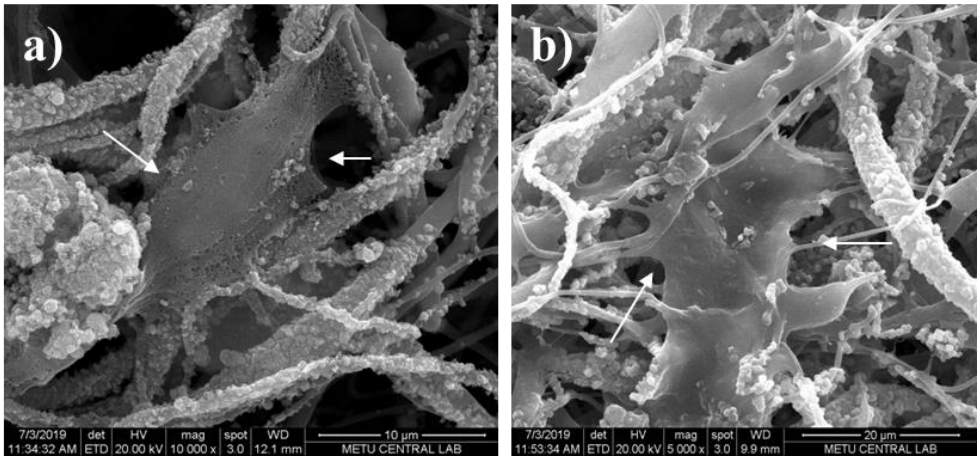


Figure 3.37. SEM images of Saos-2 cells on PCL/90HA10AKR scaffolds after incubation periods; 7 days a) (10 000 x), 14 days b) (5 000 x). (Arrows: Spread cells).

# CHAPTER 4

# CONCLUSION

Bone tissue damages are occurring at very high numbers worldwide each year as a result of many conditions like accidents, disease etc. This study investigated synthesis and characterization of a less investigated of AKR and its combinational forms with well known bioceramics (HA and CHA) for the first time in literature. Using synthesized forms, PCL-bioceramic scaffolds were produced by wet electrospinning technique and these scaffolds were investigated for their potency on bone tissue engineering applications. Characterization methods proved that the minerals were produced successfully. *In vitro* studies of minerals represented that all minerals promote mineralization with AKR having higher mineralization than the others. Mineral loaded into PCL scaffolds showed that presence of either CHA or AKR enhanced CaP precipitation on the composite scaffolds. *In vitro* cell culture studies demonstrated that HA, CHA and AKR presence provided proliferation and differentiation of osteoblastic cells in osteoinductive environment. As a summary, produced scaffolds loaded by biocompatible and bioactive mineral composites promise to support bone tissue regeneration.

## REFERENCES


Amoros, J.L., Cantavella, V., Jarque, J.C., & Feliu, C. 2008. Green strength testing of pressed compacts: An analysis of the different methods, Journal of the European Ceramic Society, 28. 701–710.

Arkadani, H., Behnam-Ghader, A. A., Hesaraki, S., & Abbasi-Shahni, M. 2011. Mechanical properties and in vitro bioactivity of β-tri calcium phosphate, merwinite nanocomposites, Key Engineering Materials, (493-494). 582-587.

Asmatulu, R. 2012. Nanocoatings for corrosion protection of aerospace alloys. Woodhead Publishing Series in Metals and Surface Engineering, 357-374.

Atila, D., Keskin, D., & Tezcaner, A. 2015. Cellulose acetate based 3-dimensional electrospun scaffolds for skin tissue engineering applications, Carbohydrate Polymers, 133. 251-261.

Atkins G. J., Findlay D. M., Anderson P. H., & Morris H.A. 2011. Target genes: bone proteins, Vitamin D (Third Edition), Feldman, D., Adams, J., Pike, J. 411-424, Australia: Academic Press.

Bakhsheshi-Rad, H. R., Hamzah, E., Ismail, A. F., Aziz, M., Najafinezdah, A., & Daroonparvar, M. 2019a. Synthesis and in-vitro performance of nanostructured monticellite coating on magnesium alloy for biomedical applications, Journal of Alloys and Compounds, 773. 180-193.

Bakhsheshi-Rad, H. R., Akbari, M., Ismail, A., Aziz, M., Hadisi, Z., Pagan, E., Daroonparvar, M., & Chen, X. 2019b. Coating biodegradable magnesium alloys with electrospun poly-L-lactic acid-åkermanite-doxycycline nanofibers for enhanced biocompatibility, antibacterial activity, and corrosion resistance, Surface and Coatings Technology, 377. 124898.

Bala, Y., & Seeman, E. 2015. Bone's material constituents and their contribution to bone strength in health, disease, and treatment. Calcified Tissue International, 97(3). 308-326.

Balagangadharan, K., Dhivya, S., & Selvamurugan, N. 2017. Chitosan based nanofibers in bone tissue engineering, International Journal of Biological Macromolecules, 104. 1372-1382.

Basar, B. 2009. Structural, mechanical and biocompatibility investigations of yttrium and fluoride doped nanohydroxyapatite, MSc Thesis, Middle East Technical University, Turkey.

Bigi, A., Foresti, E., Gregorini, R., Ripamonti, A., Roveri, N., & Shah, J.S. 1992. The role of magnesium on the structure of biological apatites, Calcified Tissue International, 50. 439-444.

Boskey A. L., & Robey P. G. 2013. Osteoporosis 4th ed., Marcus, R., Dempster, D., Cauley, J., Feldman, D., Luckey, M. The regulatory role of matrix proteins in mineralization of bone. 235-255. United States: Academic Press. USA.

Bosworth, L.A., & Downes, S. 2010. Physicochemical characterisation of degrading polycaprolactone scaffolds, Journal of Polymer Degradation and Stability, 95. 2269-2276.

Bölgen N., Menceloglu YZ., Acatay K., Vagel I., & Piskin E. 2005. In vitro and in-vivo degradation of non-woven materials made of poly (ε-caprolactone) nanofibers prepared by elecrospininning under different conditions, Journal of Biomaterials Science Polymer, 16(12). 1537-1555.

Callister, J., & William, D. 2007. Materials Science and Engineering, John Wiley & Sons, Inc., 7th ed.

Capuccini, C., Torricelli, P., Boanini, E., Gazzano, M., Giardino, R., & Bigi, A. 2009. Interaction of Sr-doped hydroxyapatite nanocrystals with osteoclast and osteoblast-like cells, Journal of Biomedical Materials Research Part A, 89 (3). 594-600.

Chen, L., Zhai, Dong., Wu, C., & Chang, J. 2014. Poly(d, l-lactic)-reinforced akermanite bioceramic scaffolds: Preparation and characterization, Ceramics International, 40(8). 12765-12775.

Chen, F.-M., & Liu, X. 2016. Advancing biomaterials of human origin for tissue engineering, Progress in Polymer Science, 53. 86-168.

Chen, H., Cheng J., Ran, L., Yu, K., Lu, B., Lan, G., Dai, F., & Lu, F. 2018. An injectable self-healing hydrogel with adhesive and antibacterial properties effectively promotes wound healing, Carbohydrate Polymers, 201. 522-531.

Chen, X., Ou, J., Kang, Y., Huang, Z., Zhu, H., Yin, G., & Wen H. 2007. Synthesis and characteristics of monticellite bioactive ceramic, Journal of Materials Science: Materials in Medicine, 19(3). 1257–1263.

Dalgic, A.D., Alshemary, A.Z., Tezcaner, A., Keskin, D., & Evis, Z. 2018. Silicate-doped nano-hydroxyapatite/graphene oxide composite reinforced fibrous scaffolds for bone tissue engineering, Biomaterials Applications, 32(10). 1392-1405.

Dalton, P. D., Joergensen, N. T., Groll, J., & Moeller, M. 2008. Patterned melt electrospun substrates for tissue engineering, Biomedical Materials, 3. 1-11.

Diba, M., Goudouri, O.-M., Tapia, F., & Boccaccini, A. R. 2014. Magnesium-containing bioactive polycrystalline silicate-based ceramics and glass-ceramics for biomedical applications, Current Opinion in Solid State and Materials Science. 3(3). 221-253.

Dorozhkin, S. V. 2015. Calcium orthophosphate bioceramics, Ceramics International, 41. 13913-13966.

Elmagd, M. A. 2016. Common sports injuries, International Journal of Physical Education, Sports and Health, 3. 142-148.

Encylopedia of Britannica Inc., Heaney, R.P., Whedon, G.D. from[https://www.britannica.com/science/bone-remodeling].

Esmailian, S., Irani, S., Bakhshi, H., & Zandi, M. 2018. Biodegradable bead-on-spring nanofibers releasing β-carotene for bone tissue engineering, Materials and Engineering: C, 92. 800-806.

Evis, Z., & Ozturk, F. 2008. Investigation of tensile strength of hydroxyapatite with various porosities by diametral strength test, Materials Science and Technology, 24. 274–278.

Ezekiel, I., Kasim, S.R., Ismail, Y.M., & Noor, A.M. 2018. Nanoemulsion synthesis of carbonated hydroxyapatite nanopowders: Effect of variant CO32-/PO43- molar ratios on phase, morphology, and bioactivity, Ceramics International, 44. 13082-13089.

Farzadi, A., Solati, M., Bakhshi, F., & Aminian, A. 2011. Synthesis and characterization of hydroxyapatite/b-tricalcium phosphate nanocomposites using microwave irradiation, Ceramics International, 37. 65-71.

Foggia, M. D., Plescia, E., Corda, U., & Torreggiani, A. 2010. Effects of sterilisation by high-energy radiation on biomedical poly-(ε-caprolactone)/hydroxyapatite composites, Journal of Materials Science: Materials in Medicine, 21(6). 1789-1797.

Gan Z., Liang Q., Zhang J., & Jing X. 1997. Enzymatic degradation of poly(e-caprolactone) film in phosphate buffer solution containing lipases. Journal of Polymer Degradation and Stability, 56. 209-213.

Glorieux F. H., Jüppner H., & Pettifor J. M. 2012. Bone matrix and mineralization. Pediatric Bone, 9-37. Canada: Academic Press.

Gordon J., Desaix P., Johnson E., Johnson J., Korol O., & Kruse D. 2016. Bone tissue and the skeletal system, Anatomy and Physiology, 34. Houston, USA.

Gu, H., Guo, F., Zhou, X., Gong, L., Zhang, Y., Zhai, W., Chen L., Cen L., Yin S., Chang J., & Cui L. 2011. The stimulation of osteogenic differentiation of human adipose-derived stem cells by ionic products from akermanite

dissolution via activation of the ERK pathway, Biomaterials, 32(29). 7023-7033.

Hafezi, M., Talebi, A. R., Miresmaeili, S. M., Sadeghian, F., & Fesahat, F. 2013. Histological analysis of bone repair in rat femur via nanostructured merwinite granules. Ceramics International, 39(4). 4575–4580.

Hall B. K. 2015. Osteoblast and osteocyte diversity and osteogenesis in vitro, Bones and Cartilage, 401-413. Canada: Academic Press.

Hambli, R., & Hattab, N. 2013. Application of neural network and finite element method for multiscale prediction of bone fatigue crack growth in cancellous bone, Multiscale Computer Modeling in Biomechanics and Biomedical Engineering, 14. 3-30.

Hench, L. L., & West, J. K. 1990. The sol-gel process, Chemical Reviews, 90(1). 33-72.

Hochberg, M.C., Smolen, J.S., Weisman, M.H., Silman, A.J., & Weinblatt, M.E. 2015. Bone structure and function, Rheumatology, 42-55. United States: Mosby.

Huang, X.-H., & Chang, J. 2008. Preparation of nanocrystalline bredigite powders with apatite-forming ability by a simple combustion method, Materials Research Bulletin, 43(6). 1615-1620.

Huang, Y., Jin, X., Zhang, X., Sun, H., Tu, J., Tang, T., Chang J., & Dai K. 2009. In vitro and in vivo evaluation of akermanite bioceramics for bone regeneration, Biomaterials, 30(28). 5041–5048.

Huang, Y., Wu, C., Zhang, X., Chang, J., & Dai, K. 2018. Regulation of immune response by bioactive ions released from silicate bioceramics for bone regeneration, Acta Biomaterialia, 15(66). 81-92.

Iwata, N., Lee, G., Tokuoda, Y., & Kawashima, N. 2004. Sintering behavior and apatite formation of diopside prepared by coprecipitation process, Colloids Surf B Biointerfaces, 34(4). 239-245.

Jain, A., Khan, W., & Kyziot, A. 2019. Particulate systems of PLA and its copolymers, Materials for Biomedical Engineering, 21(23). 349-380.

Kalantari, E., Naghib, S. M., Naimi-Jamal, M. R., Esmaeili, R., Majidzadeh-A, K., & Mozafari, M. 2018. Nanostructured monticellite: An emerging player in tissue, Materials Today, 5(7). 15744–15753.

Kamst, G.F., Vasseur, J., Bonazzi, C., Bimbenet, J.J. 1999. A new method for the measurement of the tensile strength of rice grains by using the diametral compression test" Journal of Food Engineering, 40. 227-232.

Kharaziha, M., & Fathi, M. H. 2010. Improvement of mechanical properties and biocompatibility of forsterite bioceramic addressed to bone tissue engineering, Journal of the Mechanical Behaviour of Biomedical Materials, 3(7). 530-537.

Kim, H. L., Jung, G. Y., Yoon, J. H., Han, J. S., Park, Y. J., Kim, D. G., Zhang M., & Kim D.J. 2015. Preparation and characterization of nano-sized hydroxyapatite/alginate/chitosan composite scaffolds for bone tissue engineering, Materials Science and Engineering C, 54, 20-25.

Kobayashi, T., Okada, K., Kuroda, T., & Sato, K. 1997. Osteogenic cell cytotoxicity and biomechanical strength of the new ceramic Diopside, Journal of Biomedical Materials Research, 37(1). 100-7.

Kokubo, T., Kushitani, H., Sakka, S., Kitsugi, T., & Yamamuro, T. 1990. Solutions able to reproduce in vivo surface-structure changes in bioactive glass-ceramic A-W, Journal of Biomedical Research, 24(6). 721-734.

Li, L., Li, G., Jiang, J., Liu, X., Luo, L., & Nan, K. 2012. Electrospun fibrous scaffold of hydroxyapatite/poly (caprolactone) for bone regeneration, Journal of Materials Science: Materials in Medicine, 23(2). 547-554.

Liao, X., Lu, Z., Liu, X., & Shi, B. 2004. Collagen fiber immobilized Myrica rubra tannin and its adsorption to UO2(2+), Environmental Science and Technology, 38(1). 324-328.

Liu, Y., Luo, D., & Wang, T. 2016. Hierarchical structures of bone and bioinspired bone, Materials Views, 12(34). 4611-4632.

LogithKumar, R., KeshavNarayan, A., Dhivya, S., Chawla, A., & Saravanan, S. 2016. A review of chitosan and its derivatives in bone tissue engineering, Carbohydrate Polymers, 151. 172-188.

Maia, M., Fernandes, G. V., Rossi, A. M., & Dias, A. P. 2008. Effect of hydroxyapatite and zinc-containing hydroxyapatite on osseous repair of critical size defect in the rat calvaria, Key Engineering Materials, 361(363). 1273-1276.

Manafi, S., Rahimiopour, M. R., Yazdani, B., & Razavi, M. 2008. Synthesis of nano-hydroxyapatite under a sonochemical/hydrothermal condition, Biomedical Materials. 3(2). 122-128.

Manoukian, O.S., Sardashti, N., Stedman, T., Gailiunas, K., Ojha A., Penalosa, A., Mancuso, C., Hobart, M., & Kumbar, S.G. 2019. Biomaterials for tissue engineering and regenerative medicine, Encyclopedia of Biomedical Engineering, 462-482.

Marcacci, M., Kon, E., Moukhachev, V., Lavroukov, A., Kutepov, S., Quarto, R., Mastrogiacomo, M., & Cancedda, R. 2007. Stem cells associated with macroporous bioceramics for long bone repair: 6- to 7-year outcome of a pilot clinical study, Tissue Engineering. 13(5). 947-955.

Marshall, W. J., Day, A.P., Lapsley, M., & Ayling, R. M. 2014. Metabolic bone disease. Clinical Biochemistry: Metabolic and Clinical Aspects, 3(3). 604-635.

Mohammad, N.F., Othman, R., Abdullah, N.A., & Yeoh, F.Y. 2016. In vitro evaluation of mesoporous carbonated hydroxyapatite in MC3T3-E1 osteoblast cells, Procedia Chemistry, 19. 259-266.

Moorthi, A., Parihar, P.R., Saravanan, S., Vairamani M., & Selvamurugan N. 2014. Effects of silica and calcium levels in nanobioglass ceramic particles on osteoblast proliferation. Materials Science and Engineering C, 43. 458-464.

Morais, S. (2011). Porosity of fiber mats from different polymer solutions - evaluating the influence of process and solution parameters, 9. MSc thesis, Hannover University, Germany.

Motamedian, S. R., Hosseinpour, S., Ahsaie, M. G., & Khojasteh, A. 2015. Smart scaffolds in bone tissue engineering: A systematic review of literature, World Journal of Stem Cells, 7(3). 657-668.

Muruganandan, S., Roman A.A., Sinal C.J. 2009. Adipocyte differentiation of bone marrow-derived mesenchymal stem cells: Cross talk with the osteoblastogenic program, Cellular and Molecular Life Sciences CMLS, 66(2). 236-253.

Najafinezdah, A., Abdellahi, M., Ghayour, H., Soheily, A., Chami, A., & Khandan, A. 2017. A comparative study on the synthesis mechanism, bioactivity and mechanical properties of three silicate bioceramics, Materials Science and Engineering C, 72. 259-267.

Nga, NK., Leoni, M., Maniglio, D., & Migliaresi, C. 2012. Hydroxyapatite nanorods: Soft-template synthesis, characterization and preliminary in vitro tests, Journal of Biomaterials Applications, 28(1). 49-61.

Ni, Q., Santos, A. D., Lam, H., & Qin, Y.X. 2007. Assessment of simulated and functional disuse on cortical bone by nuclear magnetic resonance, Advances in Space Research, 40(11). 1703–1710.

Niranjan, R., Koushik, C., Saravanan, S., Moorthi, A., Vairamani, M., & Selvamurugan, N. 2013. A novel injectable temperature-sensitive zinc doped chitosan/-glycerophosphate hydrogel for bone tissue engineering, International Journal of Biological Macromolecules, 54. 24-29.

Okada, M., & Matsumoto, T. 2015. Synthesis and modification of apatite nanoparticles for use in dental and medical applications, Japanese Dental Science Review, 51. 85-95.

Osta, B. 2014. Effects of Interleukine – 17A (II-17A) and tumor necrosis factor alpha (TNF-α) on osteoblastic differentiation, Journal of Frontiers in Immunology, 6. 151-161.

Ou, J., Kang, Y., Huang, Z., Chen, X., Wu, J., Xiao, R., & Yin G. 2008. Preparation and in vitro bioactivity of novel merwinite ceramic, Biomedical Materials, 3(1). 1-8.

Pina, S., Vieira, S., Rego, P., & Torres, P. M. 2010. Biological responses of brushite-forming Zn-and ZnSr-substituted-Tricalcium phosphate bone cements, European Cells & Materials, 20. 162-177.

Porter, A. E., Patel, N., Skepper, J. N., Best, S. M., & Bonfield, W. 2003. Comparison of in vivo dissolution processes in hydroxyapatite and silicon-substituted hydroxyapatite bioceramics, Biomaterials, 24(25). 4609-4620.

Price, C., Langford, J., & Koval, K. 2013. Silicon: A review of its potential role in the prevention and treatment of postmenopausal osteoporosis, International Journal of Endocrinology, 11.

Rahaman, MN, Xiao, W., & Huang, W. 2017. Bioactive glass composites for bone and musculoskeletal tissue engineering, Bioactive Glasses, (285-336). 2355-2373.

Rahmati, M., Fathi, M., & Ahmadian M. 2018. Preparation and structural characterization of bioactive bredigite (Ca7MgSi4O16) nanopowder, Journal of Alloys and Compounds, 732. 9-15.

Rao, S. H., Harini, B., Shadamarshan, R. P., Balagangadharan, K., & Selvamurugan, N. 2017. Natural and synthetic polymers/bioceramics/bioactive compounds-mediated cell signalling in bone tissue engineering, International Journal of Biological Macromolecules, 110. 88-96.

Robey P. G. 2008. Noncollagenous bone matrix proteins. Principles of Bone Biology, 1. 335-349.

Saad, B. & Suter, U.W. 2001. Biodegradable polymeric materials, Encyclopedia of Materials: Science and Technology (Second Edition), 551-555.

Schiller, C., & Eppe, M. 2003. Carbonated calcium phosphates are suitable pH-establishing fillers for biodegradable polyesters, Biomaterials, 24(12). 2037-2043.

Schumacher, M., Wagner, A. S., Himmelreich, J. K., Bernhardt, A., Rohnke, M., & Wenisch, S. 2016. Strontium substitution in apatitic CaP cements effectively attenuates osteoclastic resorption but does not inhibit osteoclastogenesis, Acta Biomaterialia, 37. 184–194.

Sethu, S. N., Namashivayam, S., Devendran, S., Nagarajan, S., Tsai, W.-B., Narashiman, S., Ramachandaran M., & Ambigapathi M. 2017. Nanoceramics on osteoblast proliferation and differentiation in bone tissue engineering, International Journal of Biological Macromolecules, 98. 67-74.

Shanmugam, M., & Roman, A. A. 2008. Adipocyte differentiation of bone marrow-derived mesenchymal stem cells: Cross talk with the osteoblastogenic program, Cellular Molecular Life and Sciences CMLS, 66(2). 236-253.

Shukla, A., Dasgupta, N., Ranjan, S., Singh, S., & Chidambram, R. 2017. Nanotechnology towards prevention of anaemia and osteoporosis: from concept to market, Journal of Biotechnoloy & Biotechnologycal Equipment, 31(5). 863-879.

Song, H. H., Yoo, M. K., Moon, H. S., Choi, Y. J., Lee, H. C., & Cho, C. S. 2007. A novel polycaprolactone/hydroxyapatite scaffold for bone tissue engineering, Key Engineering Materials, (342-343). 265-268.

Soundarya, P., Sanjay, V., Menon, H., Dhivya, S., & Selvamurugan, N. 2018a. Effects of flavonoids incorporated biological macromolecules based scaffolds in bone tissue engineering, International Journal of Biological Macromolecules, 110. 74-87.

Soundarya, S. P., Menon, A. H., Chandran, S. V., & Selvamurugan, N. 2018b. Bone tissue engineering: Scaffold preparation using chitosan and other biomaterials with different design and fabrication techniques, International Journal of Biological Macromolecules, 119. 1228-1239.

Speirs, A.D.,Oxland, T.R., Masri, B.A.,Poursartip, A., & Duncan, C.P. 2005. Calcium phosphate cement composites in revision hip arthroplasty, Biomaterials, 26. 7310–7318.

Stevens, M. M. 2008. Biomaterials for bone tissue engineering. Materials Today, 11(5). 18-25.

Sun, H., Wu, C., Dai, K., Chang, J., & Tang, T. 2006. Proliferation and osteoblastic differentiation of human bone marrow-derived stromal cells on akermanite-bioactive ceramics, Biomaterials, 27(33). 5651–5657.

Tavangarian, F., & Emadi, R. 2011. Mechanism of nanostructure bredigite formation by mechanical activation with thermal treatment. Materials Letters, 65(15-16). 2354-2356.

Thomas, M.B., Jarcho, M., Salsbury, R.L., Doremus, R.H. 1980. Dense hydroxylapatite: Fatigue and fracture strength after various treatments, from diametral tests. Journal of Materials Science, 15. 891-894.

Tsutsumi, S., & Nonami, T. 1999. Study of diopside ceramics for biomaterials, Journal of Materials Science: Materials in Medicine, 10(8). 475-479.

Uysal, I., Severcan, F., Tezcaner, A., & Evis, Z. (2014). Co-doping of hydroxyapatite with zinc and fluoride improves mechanical and biological properties of hydroxyapatite, Progress in Natural Science: Materials International, 24(4). 340-349.

Venkatesan, J., Bhatnagar, I., Manivasagan, P., Kang, K.-H., & Kim, S.-K. 2015. Alginate composites for bone tissue engineering: A review. International Journal of Biological Macromolecules, 72. 269-281.

Venugopal, E., Sahanand, K., Bhattacharyya, A., & Rajendran, S. 2019. Electrospun PCL nanofibers blended with Wattakaka volubilis active phytochemicals for bone and cartilage tissue engineering, Nanomedicine: Nanotechnology, Biology and Medicine, 21. 102044.

Wang G.C., Lu Z. F., & Zreiqat H. 2014. Bioceramics for skeletal bone regeneration, Bone Substitute Biomaterials, Mallick, K. 180-186.

Wang, X., Nyman, J., Dong, X., Leng, H., & Reyes, M. 2009. Fundamental Biomechanics in Bone Tissue Engineering. Morgan Publishers & CLaypool.

Wang, Y., Nugraha, B., Cai, L.-Q., & Gao, Y. 2013. Current Hydrogel Solutions for Repairing and Regeneration of Complex Tissues, Current Medicinal Chemistry, 21(22). 2480-2496.

Wu, C., & Chang, J. 2004. Synthesis and apatite-formation ability of akermanite, Materials Letters, 58(19). 2415 – 2417.

Wu, C., Chang, J., Wang, J., Nia, S., & Zhai, W. 2005. Preparation and characteristics of a calcium magnesium silicate (bredigite) bioactive ceramic, Biomaterials, 26(16). 2925–2931.

Wu, C., Ramaswamy, Y., & Zreiqat, H. 2010. Porous diopside ($CaMgSi_2O_6$) scaffold: A promising bioactive material for bone tissue engineering, Acta Biomaterialia, 6(6), 2237–2245.

Wubneh, A., Tsekoura, E. K., Ayranci, C., & Uludag, H. 2018. Current state of fabrication technologies and materials for bone tissue, Acta Biomaterialia, 80. 1-30.

Xia, L., Zhang, Z., Chen, L., Zhang, W., Zeng, D., Zhang, X., Chang J., & Jiang X. 2011. Proliferation and osteogenic differentiation of human periodontal ligament cells on akermanite and β-TCP bioceramics, European Cells and Materials, 22. 68-83.

Xing, M., Wang, X., Wang, E., Gao, L., & Chang, J. 2018. Bone tissue engineering strategy based on the synergistic effects of silicon and strontium ions, Acta Biomaterialia, 72. 381-395.

Xu, H.H.K., Carey, L.E., Simon Jr., C.G., Takagi, S., & Chow, L.C. 2007. Premixed calcium phosphate cements: Synthesis, physical properties, and cell cytotoxicity, Dental Materials, 23. 433-441.

Yang, W., Yang, F., Wang, Y., Both, S. K., & Jansen, J. A. 2013. In vivo bone generation via the endochondral pathway on three-dimensional electrospun fibers, Acta Biomaterialia, 9(1). 4505-4512.

Yong, W.Y., & Noor, A.F. (2016). Synthesis and sintering-wet carbonation of nano-sized carbonated hydroxyapatite, Procedia Chemistry, 19. 98-105.

Yu, H., Jang, H., Kim, T., Lee, H., & Kim, H. 2009. Apatite-mineralized polycaprolactone nanofibrous web as a bone tissue regeneration substrate, Journal of Biomedical Materials Research Part A., 88(3). 747-754.

Zhai, W., Lu, H., Wu, C., Chen, L., Lin, X., Naoki, K., Chen G., & Chang J. 2013. Stimulatory effects of the ionic products from Ca-Mg-Si bioceramics on both osteogenesis and angiogenesis in vitro, Acta Biomaterialia, 9(8). 8004-8014.

Zhu, Q.-X., Li, Y.-M., & Han. D. 2015. Co-substitution of carbonate and fluoride in hydroxyapatite: effect on substitution type and content, Frontier Materials Science, 9. 19.

Zreiqat, H., Howlett, C.R., Zannettino, A., Evans, P., Schulze-Tanzil, G., & Knabe, C. 2002. Mechanisms of magnesium-stimulated adhesion of osteoblastic cells to commonly used orthopaedic implants, Journal of Biomedical Materials Research, 62(2). 175-184.

# APPENDICES

## A. Diametral Compression Graph of HA Ceramic

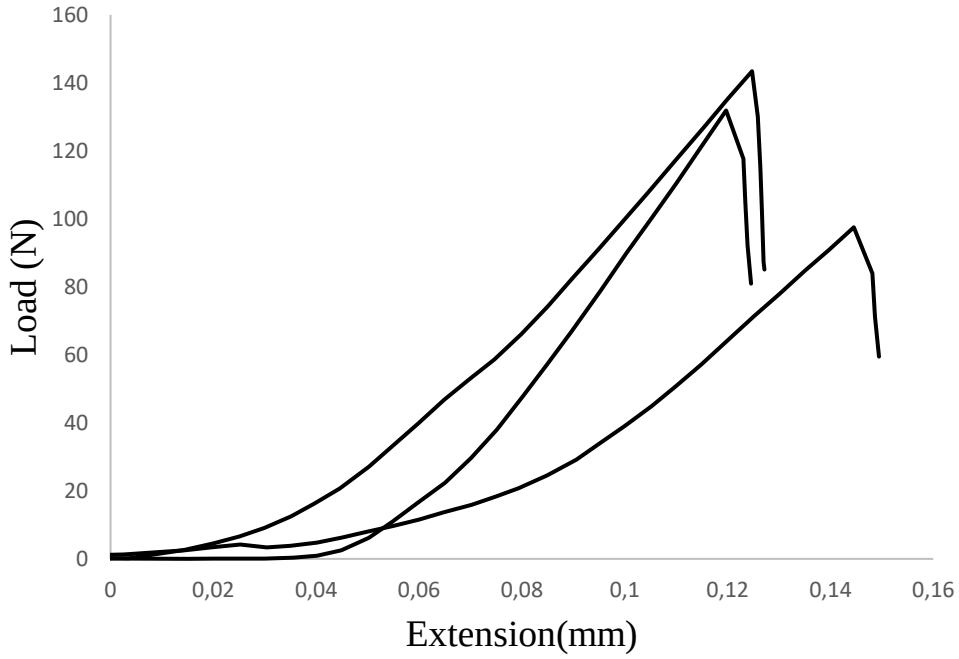

**B. Diametral Compression Graph of AKR Ceramic**

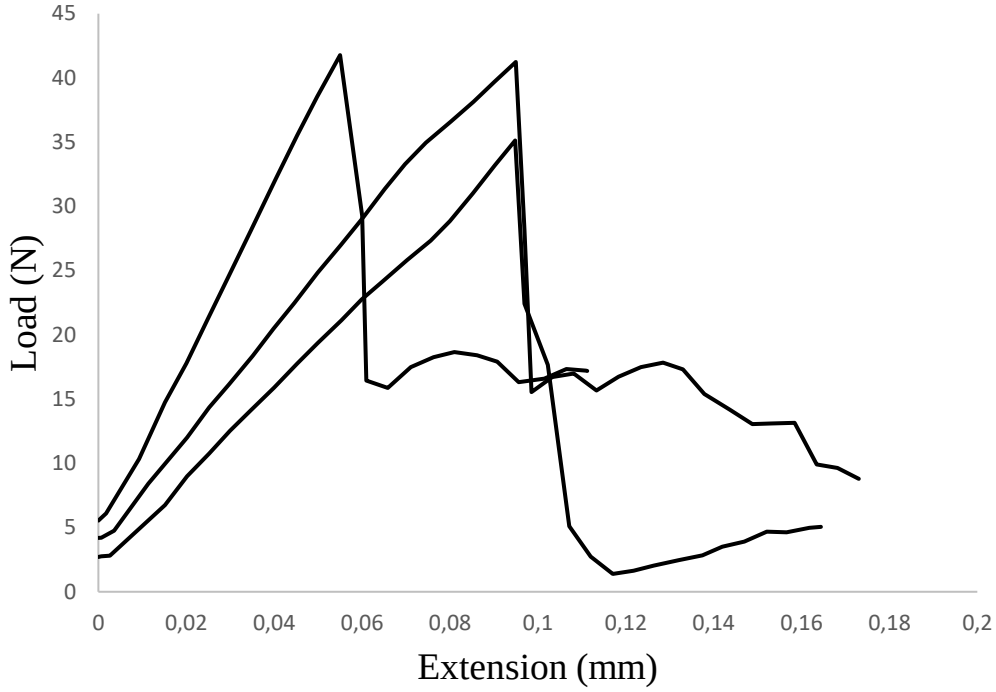

## C. Diametral Compression Graph of CHA Ceramic

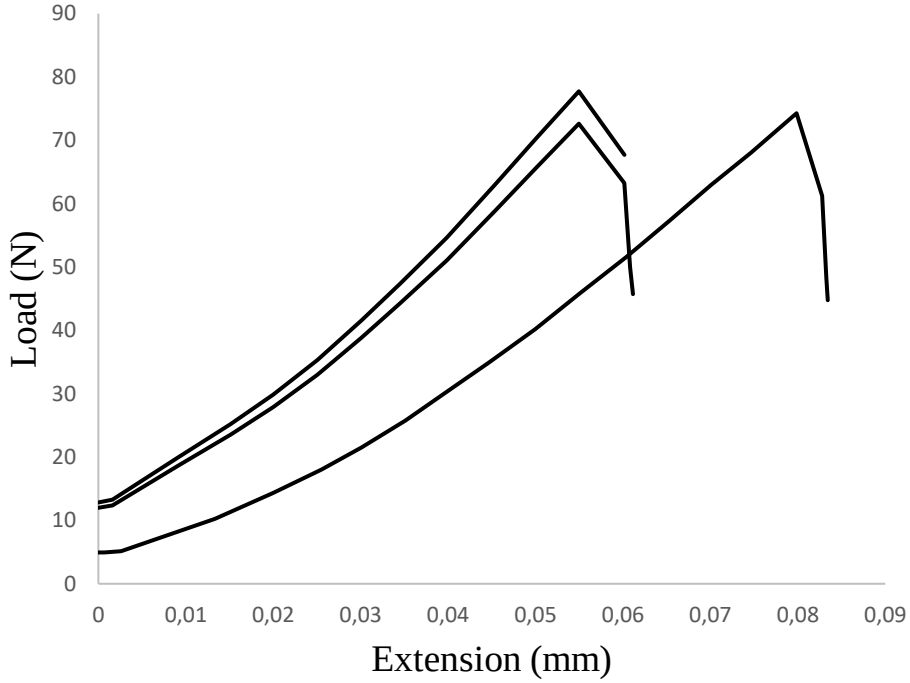

## D. Diametral Compression Graph of 90HA10AKR Composite

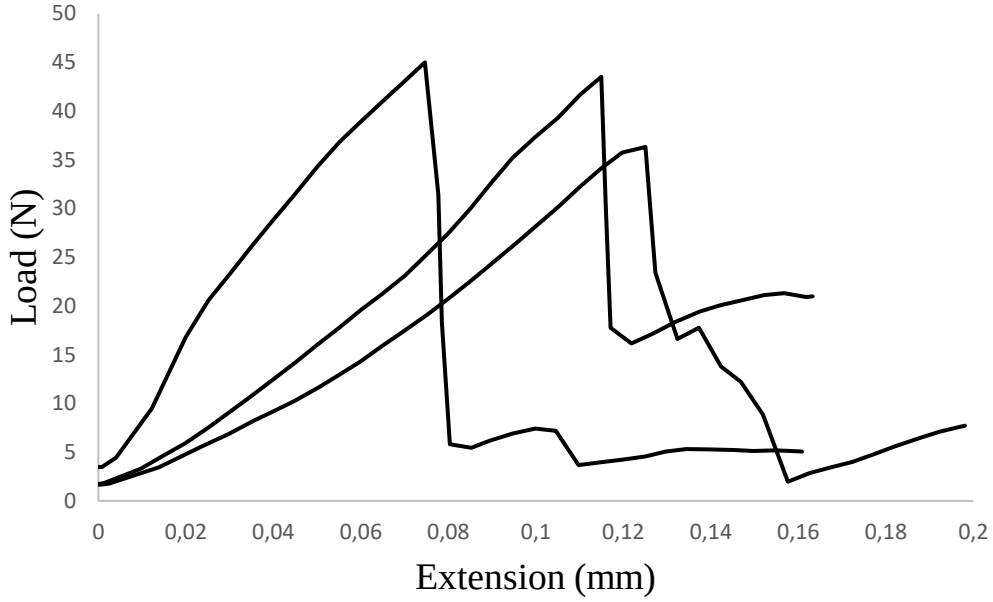

## E. Diametral Compression Graph of 90CHA10AKR Composite

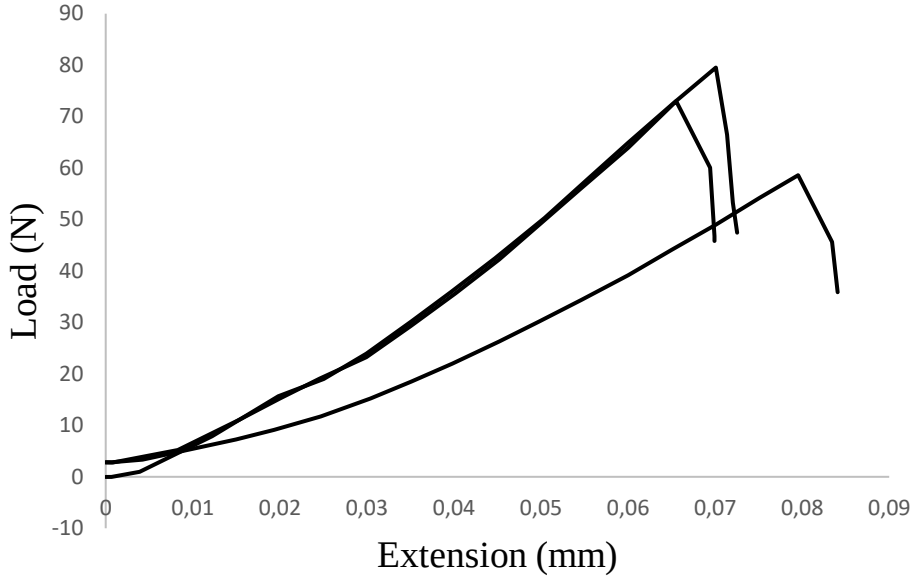

## F. Calibration Curve for ALP Activity Assay